

Identification and analysis of long-duration low-frequency events from microseismic data

A Thesis
Presented to
the Faculty of the Department of Earth and Atmospheric Sciences
University of Houston

In Partial Fulfillment
of the Requirement for the Degree
Master of Science

By
Hongru Hu
May 2015

Identification and analysis of long-duration low-frequency events from microseismic data

Hongru Hu

APPROVED:

Dr. Aibing Li

Department of Earth and Atmospheric Sciences

Dr. Stuart Hall

Department of Earth and Atmospheric Sciences

Dr. Jie Zhang

GeoTomo, LLC

Dean, College of Natural Sciences and Mathematics

Acknowledgement

I would like to thank my advisor Dr. Aibing Li for her great idea about this research as well as the time, efforts, and patience for helping me. I would also like to thank my committee member Dr. Stuart Hall and Dr. Jie Zhang for their suggestions and revising for the thesis.

Secondly, I want to thank Pemex Exploration & Production for releasing the data to me.

Finally, I want to thank my father Yawu Hu, my mother Linxia Wang, and my wife Yuexing Qian for their encouragement and support.

Identification and analysis of long-duration low-
frequency events from microseismic data

An Abstract of a Thesis
Presented to
the Faculty of the Department of Earth and Atmospheric Sciences
University of Houston

In Partial Fulfillment
of the Requirement for the Degree
Master of Science

By
Hongru Hu
May 2015

Abstract

Hydraulic fracturing is commonly used to enhance rock permeability in unconventional reservoirs. Locating microseismic events has become a standard tool in monitoring the fracturing process. However, the relation between microseismicity and crack networks has not been well understood. In addition, microseismic energy is almost negligible compared with the total energy used in fracturing. Long-duration and low-frequency (LDLF) seismic events, which are often observed in volcanic fields, have been reported from the data recorded during hydraulic fracturing. Although the origin of low-frequency events could be complicated, fluid pressurization through cracks, which is a common source for volcanic tremors, could be one main mechanism for LDLF events during hydraulic fracturing. Therefore, investigating the LDLF events from microseismic data would help to understand different types of ground deformation and help to characterize the formation of fracture network.

In this research, I have identified several LDLF events using frequency-time plots from a microseismic dataset acquired by surface receivers in the Eagle Ford Shale in Mexico. Seismograms are filtered and their envelopes are calculated. Arrivals from each energy pack are picked from the envelopes using a cross-correlation method. These arrivals are then used to locate the event through a grid-search approach. The LDLF events can be categorized in two types. Type 1 events are located at around 1500 m in depth, close to the horizontal well. The associated phase arrivals show typical P-wave moveout trends. In addition, these

events tend to migrate away from the treatment well with time. Type 1 events are probably caused by fluid pressurization in fractures. Type 2 events are located near the surface and the waves travel at a Rayleigh wave speed. The source mechanism of type 2 events is not clear, but could be related to vibrations of the operation equipment.

Contents

Abstract.....	v
Chapter 1. Introduction	1
1.1 Volcanic and tectonic LDLF events.....	2
1.2 Long-period seismic events during hydraulic fracturing.....	4
1.3 Motivation and objectives.....	7
Chapter 2. Background and description of the data.....	9
Chapter 3. Signal identification and data process.....	11
3.1 Noise reduction.....	11
3.2 LDLF signal identification.....	12
3.3 Data analysis.....	24
3.4 Traveltime picking for the LDLF events.....	27
Chapter 4. Locating the LDLF events by grid search method.....	38
4.1 The grid search method.....	38
4.2 Velocity model and geometry.....	38
4.3 Locating results.....	39
4.4 Error estimation of the locations.....	43
Chapter 5. Discussion.....	49
Chapter 6. Conclusions.....	52
Bibliography.....	54

Chapter 1. Introduction

Hydraulic fracturing is a common technique used to increase permeability and production of unconventional reservoirs. Large volumes of fluids are injected into the reservoir, often through deviated or horizontal wells (Fig 1). Increasing fluid pressure

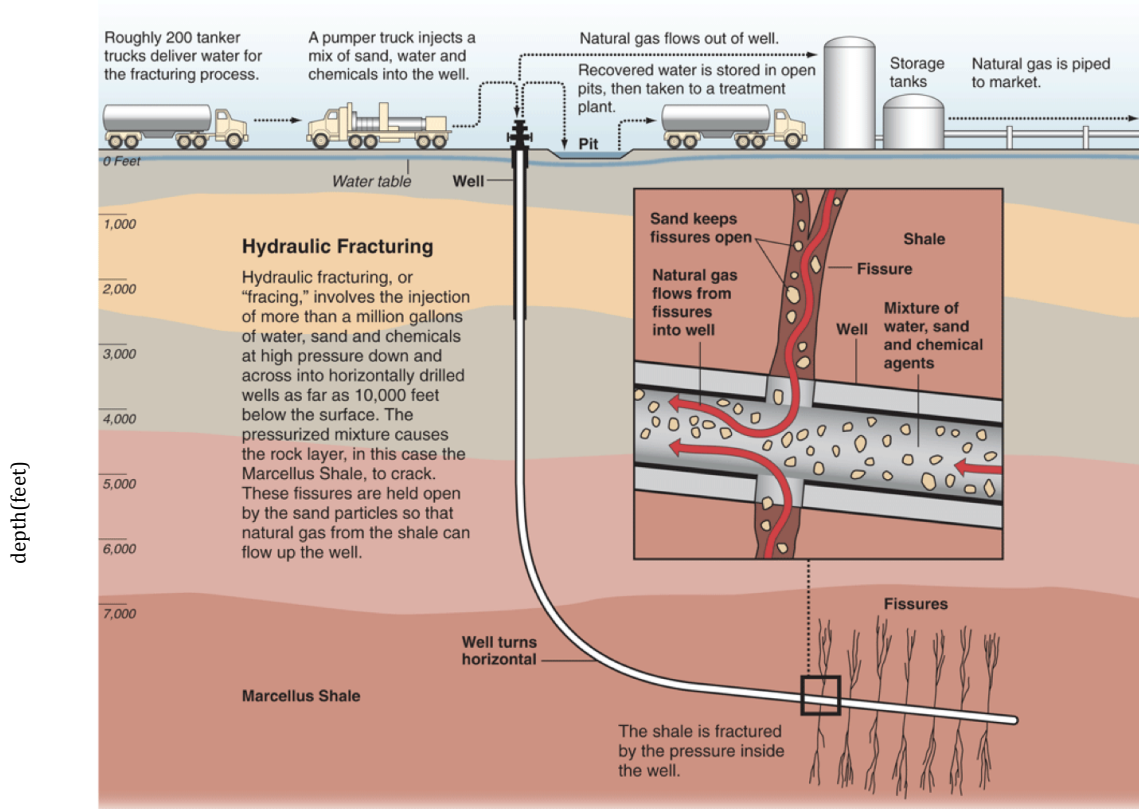


Fig 1. The fundamental steps in hydraulic fracture process (Granberg, 2010)

alters the local stress field and causes the rock to fail, which generates cracks and produces microseismic events. Therefore, mapping the locations of microseismic events becomes a standard tool in monitoring the fracturing process. However, as pointed out by Maxwell and Cipolla (2011) and Warpinski et al. (2013), the dominant fast shear deformation associated with microseismic sources (with the average

magnitude of -2) does not provide much information for the growth of hydraulic fractures that are associated with tensile stress and volume change. Microseismic energy is an insignificant portion of the total injection energy, suggesting other types of deformation beyond shear failure must exist. This is confirmed by long-period, aseismic micro-deformation that was measured from tiltmeters during the fracture treatment in the Eagle Ford shale (Astakhov et al., 2012; Walser and Roadarmel, 2012). In addition, long-period seismic events and tremors were reported for several fracture simulations (Zoback et al., 2012; Das and Zoback, 2013; Yu and Zhang, 2013; Tary et al., 2014). These long-duration low-frequency (LDLF) events can account for much higher seismic energy than unconventional microseismic sources. These studies interpreted the sources of the LDLF events by completely different mechanisms. More data and studies are required to understand the physical process of the LDLF events and characterize their usage in petroleum exploration.

1.1 Volcanic and tectonic LDLF seismic events

Long-period seismic events and tremors have been observed and studied in volcanic and hydrothermal fields for several decades (Aki et al., 1977; Kieffer, 1984; Chouet, 1988; Chouet, 1996; Almendros et al., 2001; Lesage et al., 2006; Ogiso and Yomogida, 2012; Richardson and Waite, 2013). The long-period (LP) events have a dominant frequency range of 0.1-9 Hz, which is generally lower than that of earthquakes (McNutt, 1992; Konstantinou and Schlindwein, 2002). These events can be distinguished from high-frequency earthquakes by its long duration. The seismic signals of an LP event can last from tens of seconds to a few minutes (McNutt,

1996; Chouet, 1996). Tremors can last from minutes to hours, days, and even years. According to McNutt (1996), most low-frequency events are caused by pressure change from bubble formation and collapse or nonlinear flow at shallow depths.

These events often have P waves but lack S waves. Tremors can be considered as a series of LP events at intervals of a few seconds. However, Chouet et al. (1997) found tremors at Stromboli volcano, Italy, are dominated by SH motion, which is explained by the resonance of a vertical magma conduit excited by degassing fluid. Chouet (1988) proposed that a very slow wave trapped in a fluid-filled crack could be the source for the LP events and tremors, which radiated both P and S waves.

In the past decade, slow earthquakes, very low-frequency earthquakes, low-frequency earthquakes (LFE), and nonvolcanic tremors (NVT) were observed in many subduction zones and at the San Andreas Fault (Dragert et al., 2001; Miller et al., 2002; Ito and Obara, 2006; Shelly et al., 2007; Shelly, 2009; Becken et al., 2011; Fletcher and McGarr, 2011), suggesting a broad frequency range of ground deformation. The LFEs and NVTs are evident as fluid-enabled slow shear slip at plate boundaries (Ide et al., 2007; Shelly et al., 2007) instead of the trapped fluid flow suggested by Katsumata and Kamaya (2003). The LFEs and NVTs reveal dominant frequencies at 1-5 Hz, similar to the volcanic long-period seismic events. The significant difference between the volcanic and tectonic LPEs is the observed seismic phases. Shear wave is commonly prominent in the LFEs while the volcanic LP events have strong P phases and often lack S waves in seismic records (Fig. 3).

It has been challenging to accurately locate long-period seismic events and tremors due to the lack of clear impulsive arrivals. With vigorous studies in LFEs and NVTs at the San Andreas Fault, several methods have been proposed to locate the

LFES and tremors. Nadeau and Guilhem (2009) cross-correlated similar energy envelopes at station pairs to obtain time difference and located the event by a grid-search method. They found the NVTs are closely located to the locked faults in Parkfield, California. Shelly (2009) used template events to identify LFES within tremors and used the locations of template events to search for events in the tremor sequences. This data analysis allowed Shelly to discover the migration of tremors along the San Andreas Fault. Zhang et al. (2010) applied a double-difference (DD) method using station-pair travel time differences to locate NVTs beneath the San Andreas Fault. This method locates multiple events in the inversion and the results are less sensitive to velocity models than the single-event location method.

1.2 Long-period seismic events during hydraulic fracturing

Long-period seismic events associated with hydraulic fracturing were reported back to 1986 by Bame and Fehler (1986) from experiments conducted in New Mexico. The waveforms of these events are mainly P-wave energy at 100-300 Hz and lack the S-wave arrivals. These frequencies are much higher than volcanic LP-LFES, but relatively low compared to microseismic events due to shear failure. A proposed source for the observed LFES is the sudden opening of a channel connected two cracks with different fluid pressure, which is more consistent with the fracturing theory about opening tensile cavities in response to fluid pressure than shear slip along faults that produce high-frequency microseismic events.

With the increasing interest in unconventional reservoirs in recent years, several studies were conducted on identifying and understanding the LPEs accompanying

hydraulic fracturing. Das and Zoback (2011, 2013a, 2013b) reported long-period and long-duration seismic events during hydraulic fracturing in a gas shale reservoir. The waveforms of these events have the dominant frequency range of 10-80 Hz and are largely composed of S waves (Fig 2). This observation is similar to tectonic tremors found at subduction zone and transform plate boundaries. Slow shear slip on existing faults that are weakened by high clay content in the rock or high fluid pressure on the faults is proposed as the source of the LP events (Zoback et al., 2012; Das and Zoback, 2013b). Yu and Zhang (2013) found LP events at 3-4 Hz and tremors with resonance frequencies at 14, 18 and 28 Hz (Fig. 3) during a hydraulic fracturing experiment in Sichuan Basin, China. They attributed the resonance

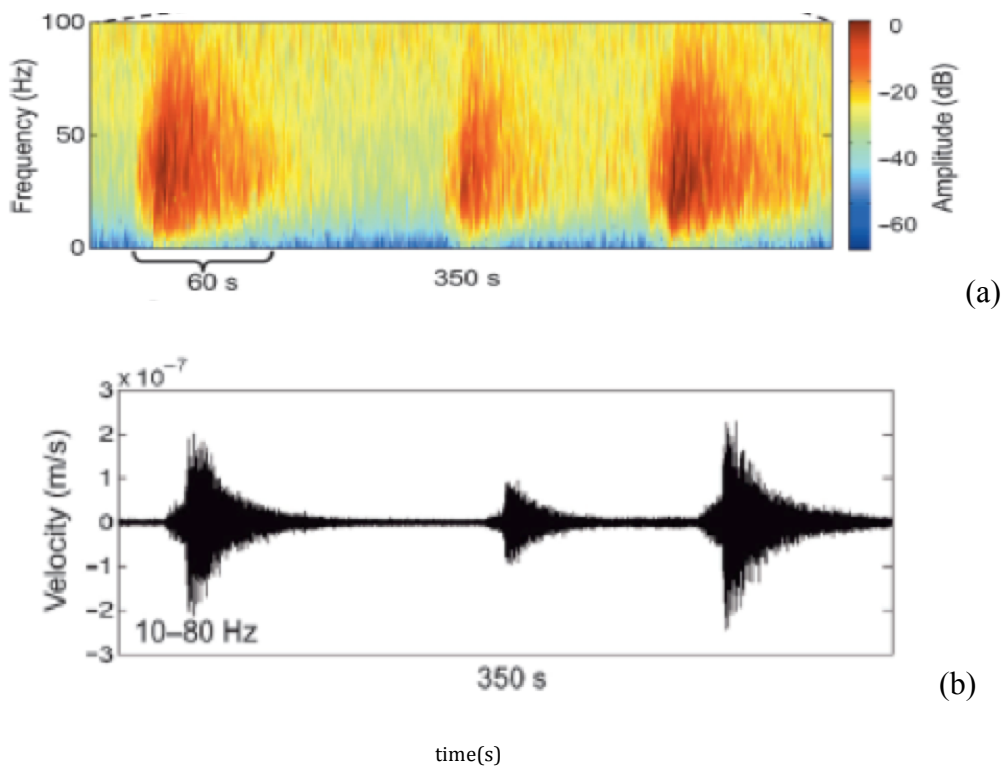


Fig 2. Long-period seismic events and tremors during hydraulic fracturing. (a) and (b) shows time-frequency spectrum and seismograms for 3 long-period events from a fracturing experiment in Barnett shale. The figures are from Das and Zoback (2013a).

frequencies to the vibration of injection pipes and interpreted the monochromatic LP events as fluid pressurization through channels or cracks. However, the locations of the LP events from this preliminary study do not match the expected fractures.

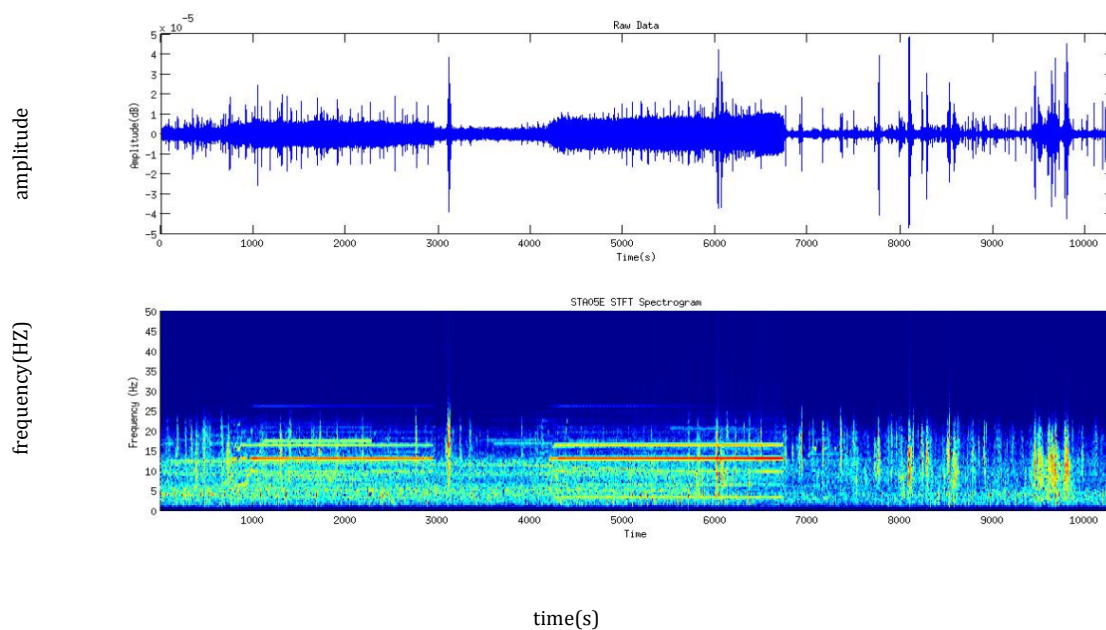


Fig 3. Three distinct resonance frequencies at 14, 18, and 28 Hz are observed during the hydraulic fracturing experiment. plus a signal at 3-4HZ which are interpreted as from the fluid flow inside the fracture (Yu and Zhang, 2013)

Tary et al., 2014 studied resonance frequencies recorded during two fracturing experiments. In one case, they found isolated resonance frequencies at ~ 8 and ~ 11 Hz and concluded that the source is from the pumping equipment or the vibrations of the vertical part of the injection well (Fig 4). In case two, they found low-frequency, long-duration signals and proposed the source as eigenvibrations of fractures or non-Darcian flow within fractures.

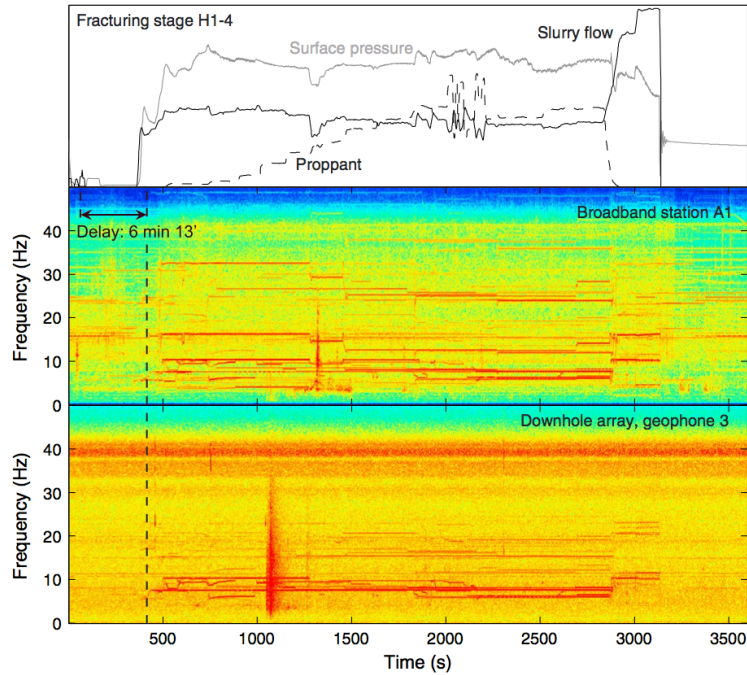


Fig 4. Treatment plot and time-frequency representation of stage H1-4 recorded by the vertical component of broad station A1 (Tary, 2013)

1.3 Motivation and objectives

Conventional microseismic events during hydraulic fracturing are caused by shear failure of rock, not directly reflect tensile fractures opened by high fluid pressure. Long-period seismic events were found in fracturing simulation and could be caused by the change of fluid pressure flow through channels and cracks, which have a potential to characterize the true fracture network. Previous studies (Das and Zoback, 2013a, Yu and Zhang, 2013, Tary et al., 2014) have shown variable seismic phases and frequency ranges in waveforms for LP events during fracture treatments. Source mechanisms of the LP events and tremors are complicated and the main hypotheses include: (1) slow shear slip on existing faults, (2) pressure change due to

fluid flow in fractures, (3) resonance of fluid-filled fractures, and (4) vibration of the injection pipe or pump.

The importance of the LDLF events in characterizing fluid flow and fracture growth and the uncertainties of the origins of the events are the motivations of this study. I will work on a microseismic data set from a hydraulic fracturing experiment in the Eagle Ford shale in Mexico. The survey consisted of more than 1000 surface receivers with a good azimuthal distribution relative to the well. I will carry out the following objectives: (1) identify LDLF events using time-frequency plots, (2) analyze frequency spectrums of the seismograms and extract the signals, (3) calculate the envelopes of seismograms and cross-correlations of the envelopes for station pairs, and (4) locate the LDLF events using a grid search method.

Chapter 2. Background and description of the data

The Eagle Ford shale is one of the most active unconventional plays in the USA. The study area is located on the Sabinas Basin at the North East Mexico in the state of Coahuila near the US and Mexico border. The microseismic data used in this research were acquired by Comesa and Microseismic Inc. The receivers were laid out at the surface directly to monitor the hydraulic fracturing covering 360 azimuth of well Montanes-1. There are 998 receivers plus 10 auxiliary receivers. The interval between each receiver is 20 m. The geometry of receivers and the treatment well is shown in Fig 5 (left), and the microseismic events located by the Microseismic Inc. for the 14 stages are shown in Fig 6 (right).

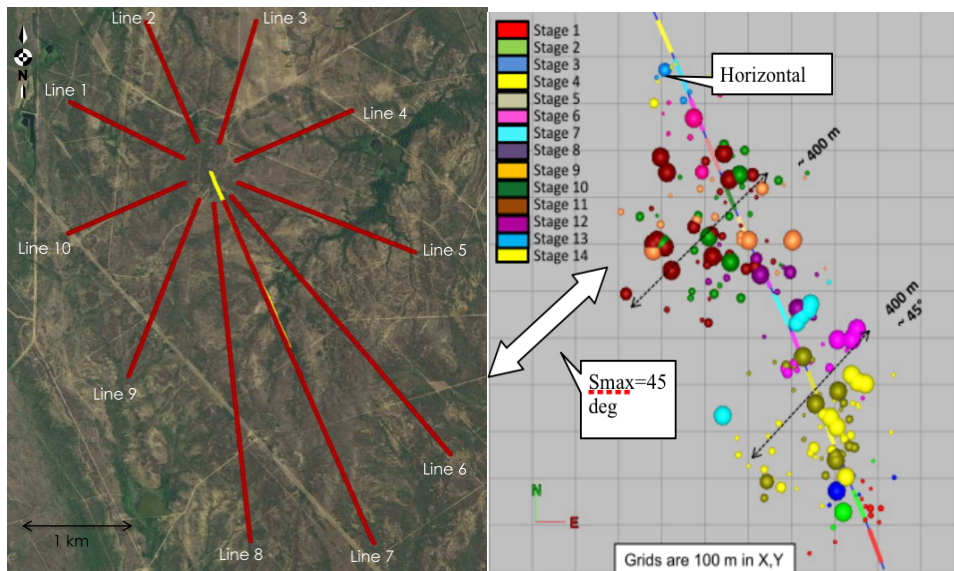


Fig 5. Left figure shows the acquisition geometry. Red lines are the layout of the receivers, and the yellow line is the location of the horizontal well. Right plot shows a map view of microseismic events at 14 stages (color coded) (Zavala-Torres, 2014)

In each of the receiver location, there were 12 folds for the receivers and the records were stacked together in order to suppress the random noise. The data were split into 13440 files and the length of file is 30s while the sampling interval is 0.002s. Unlike borehole receivers used for monitoring, these data only have vertical component.

The disadvantage of surface receivers is obvious. First of all, compared with borehole receivers, they are much further to the sources and the distance that seismic waves propagate is much longer, which may lead to the severe attenuation of high frequency signals. Secondly, near surface effects, such as the low velocity zone near the surface and the poor coupling between the receivers and the ground, make the seismic records more complicated. Thirdly, unlike the borehole receivers with 3-component data, most surface receivers only have the vertical component, which brings more challenge in locating seismic events.

Chapter 3. Signal identification and data process

3.1 Noise reduction

In microseismic survey, signal-to-noise ratio is typically much lower than in conventional seismic surveys because the energy emitted from microseismic events is very weak. Many factors may attenuate the signals, including spherical spreading, attenuation, reflection, and weathering. Eaton (2008) states that the signals recorded during microseismic surveys have relatively low magnitudes, about -2 on Richter scale. In this research, the data I use are from a surface microseismic survey, and the signal-to-noise ratio is even lower than from downhole surveys. To enhance the signal-to-noise ratio in the surface data acquisition, 10 receivers are located in the same position and the records from all 10 receivers are stacked together to suppress the random noise.

Locating the events accurately requires accurate picking of P- and S-wave first arrival. There are two common methods to pick the first arrival for P- and S-wave. One is STA/LTA and the other is modified energy ratio.

For the STA/LTA method, two windows with different length are slid across a certain trace. Equations (1), (2) and (3) are used to represent the STA/LTA approach.

$$STA(i) = \sum_{j=i}^{i-l_{sta}} \frac{a(j)^2}{l_{sta}} \quad (1)$$

$$LTA(i) = \sum_{j=i}^{i-l_{lta}} \frac{a(j)^2}{l_{lta}} \quad (2)$$

$$STA(i) = \frac{STA(i)}{LTA(i)} \quad (3)$$

In this equations, l_{sta} is the length of the STA time window while l_{lta} is the length of the LTA time window.

For the modified energy ratio method, two time windows with the same length are slid across the signal but these two time windows started at different positions.

Equations (4) and (5) represents the approach for this method.

$$ER(i) = \frac{\sum_{j=i}^{i+L} a(j)^2}{\sum_{j=i}^{i-L} a(j)^2} \quad (4)$$

$$ER3(i) = [ER(i) * abs(a(i))]^3 \quad (5)$$

For these two methods, they aim at to find out the maximum rising of the energy (Han, 2010).

3.2 LDLF signal identification

According to the previous statements, the events we are interested in should have the following features. (1) It should be long duration in time. Unlike the conventional microseismic events which are very short in time (typically less than 1ms), the events we are interested in can be as long as a couple of minutes. (2) It should have relatively narrow bandwidth and low value in frequency. Conventional microseismic events have much wider bandwidth (typically from tens of HZ to 250HZ).

The receivers keep recording during the whole process of the hydraulic fracturing. The process can be as long as a couple of days, so if we just check the data randomly, it takes too much time and work. The best way to minimize the work load

is getting more information we need from the hydraulic treatment record among which the most important data for us is the recording of treating pressure and slurry rate. The hydraulic treatment record clearly indicate when the treating process start and ends for each stage. Since we expect all our events to be recorded during the time when the formation is being treated, knowing this tremendously decreases our workload. Moreover, when the hydraulic treatment starts, there is still a long time to go before the formation start to break, so if we can identify that when the rock start to break can reduce our work even more. Fig. 6 and 7 are the plots of treating pressure and slurry rate for stage 4 and 5 respectively.

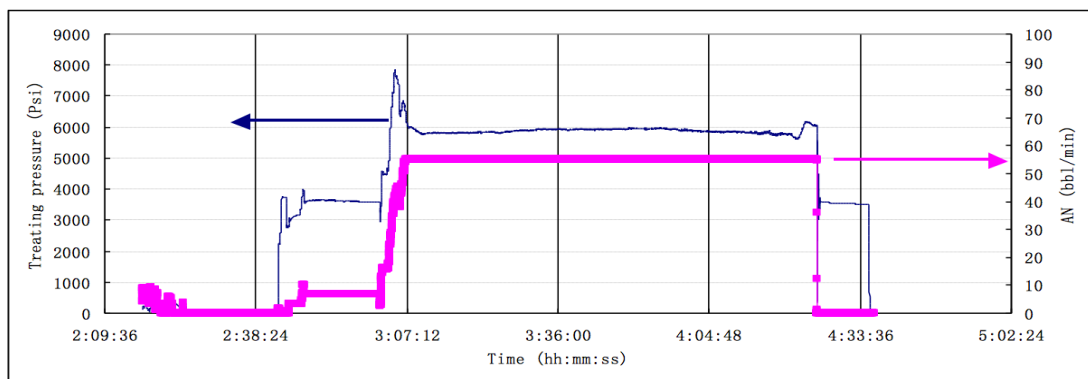


Fig 6. The plot of treating pressure and slurry rate against time for stage 4; The blue line is treating pressure and the purple line is slurry rate

For stage 4, the hydraulic treatment starts at 2:16:53 on August 29th, 2011 and last for more than two hours and ends at 4:33:36. Looking into details, before about 3:00:00, the treating pressure is going up but at around 3:00:00, the pressure drops all of a sudden to about 6000psi and the treating pressure remains at around 6000psi till about 4:25:00, during this process, the slurry rate remains stable. Therefore, we judge

that the break of the rock happened during 3:00:00 to 4:25:00 for stage 4.

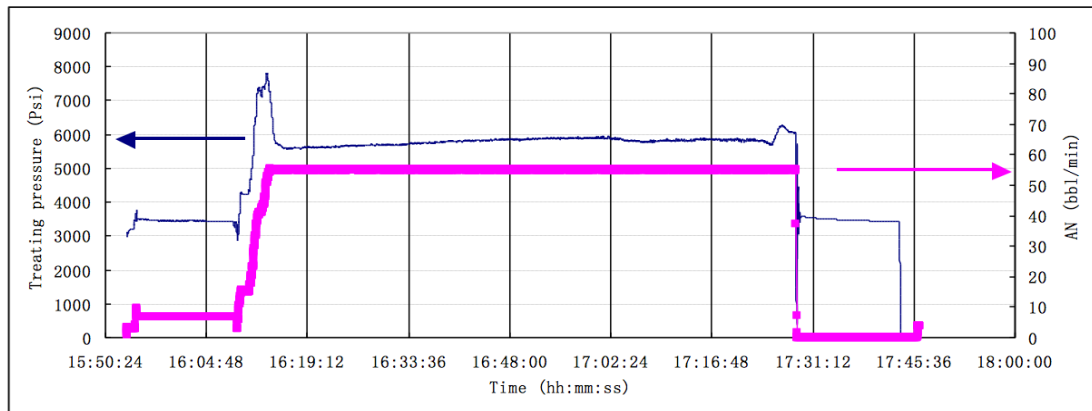


Fig 7. The plot of treating pressure and slurry rate against time for stage 5; The blue line is treating pressure and the purple line is slurry rate

Similarly, for stage 5, the break of the rock mainly happened from about 16:12:00 to 17:25:00. Based on the analysis above, we only need check the data recorded between 3:00:00 and 4:25:00 for stage4 and that recorded between 16:12:00 to 17:25:00 for stage5.

After we find some events that are possibly to be the LDLF events based on visual checking on seismograms, we need to verify the events by analyzing their frequency contents. We use the Short Term Fourier Transform (STFT) to analyze the frequency spectrum of local time sections. This method is different from the regular Fourier transform, which is applied to the whole data trace for analyzing the frequency spectrum globally. In this method, we slide a time window across the record and apply Fourier transform to the selected time window. The results are plotted as a two dimensional array with the x axis for the time and y axis for the frequency. we can see how the energy in a long duration signal changes overtime. The short time Fourier transform is calculated as:

$$STFT_f^u(t', u) = \int_t [f(t)w(t-t')]e^{-j2\pi ut} dt \quad (6)$$

where $f(t)$ is the interested signals and w is the window function, which is typically a Haan window or Gaussian window. The length of the window should be at the same scale of a period of the signal. In this research, the interested frequency ranges from about 5HZ to 30HZ corresponding to the period from 0.033s to 0.2s. Hence, the time window we used is 0.1s. The sampling interval is 0.002s, so the length of the time window is supposed to be 50 points.

Following the process above, I checked the data and found a couple of LDLF events, I'm going to locate and analysis five of the events in this research. Fig 8 shows trace 564 of the seismogram recorded from 3:30:22 to 3:42:52 and its time frequency representation. (For all the amplitude mentioned in this thesis, it means ground motion. It's the output of the receivers whose unit is volt/m/s. In industry,

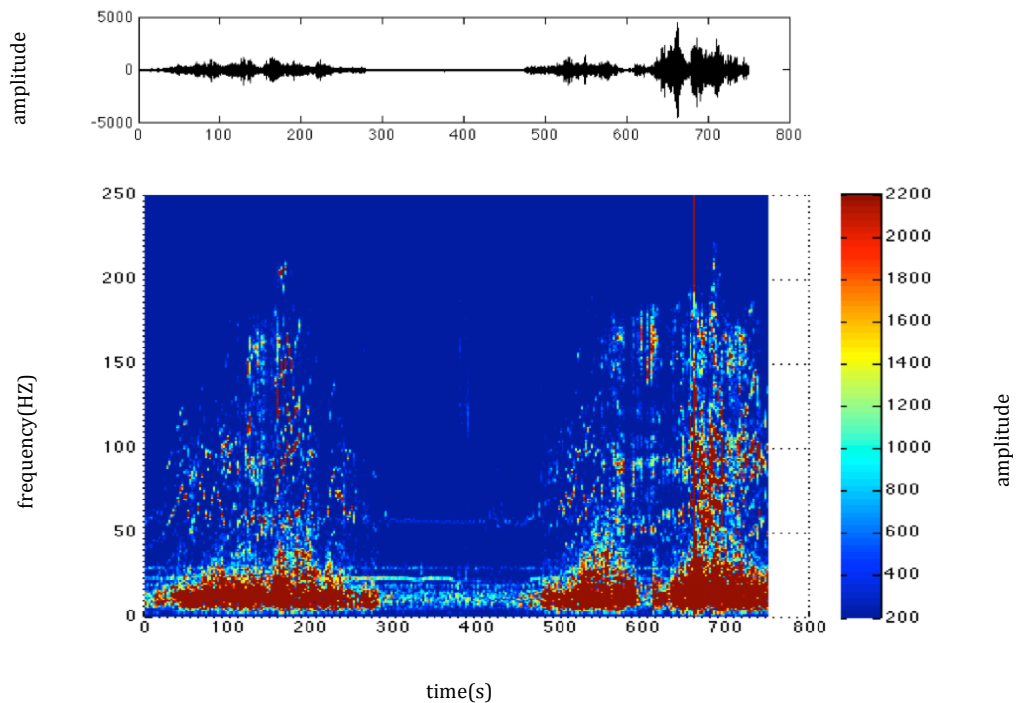


Fig 8. Seismogram and time frequency representation of trace 564 recorded from 3:30:22 to 3:42:52 on Oct 29th, 2011

typically it is treated to be dimensionless)

There are 3 LDLF events in Fig 8, one is from 0s to 290s the other are from 500s to 600s and 610s to 750s. They are named as event s4-e1, s4-e2, s4-e3 in the order of time. Fig 9 and 10 are the time slice of fig 8 at 3:32:32 (event s4-e1) and 3:39:52 (event s4-e2) . Fig 12 is the seismogram from trace 551 to 569 at a trace interval of 2.

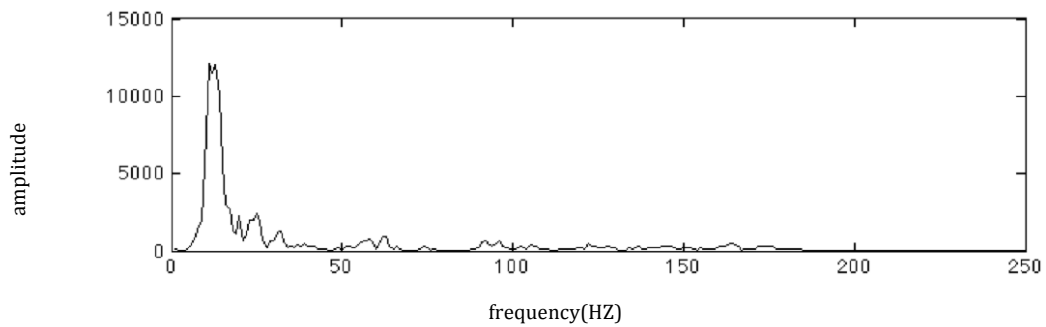


Fig 9. The frequency spectrum of trace 564 of s4-e1 at a selected time

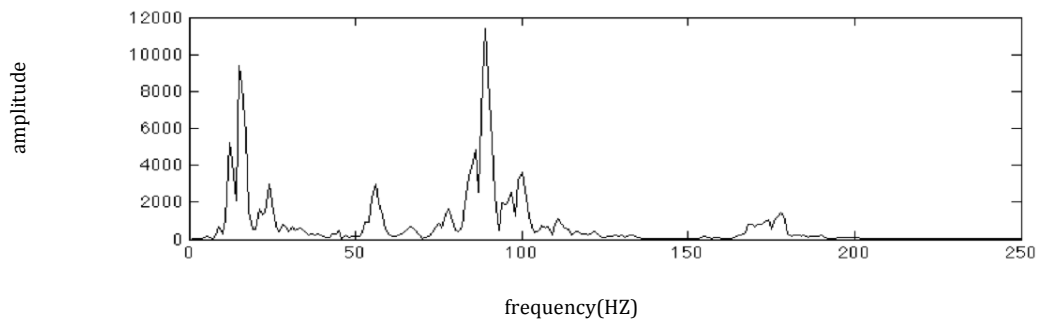


Fig 10. The frequency spectrum of trace 564 of s4-e3 at a selected time

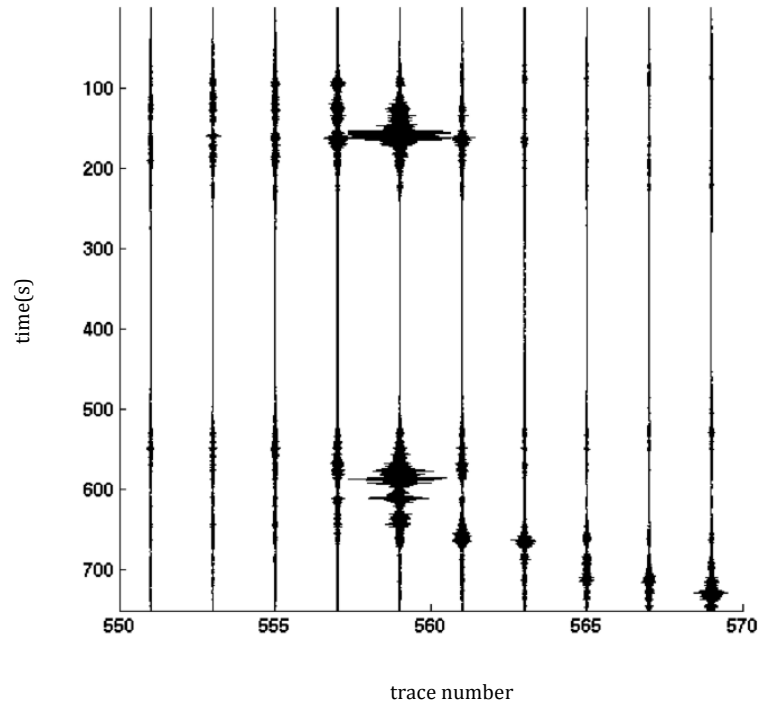


Fig 11. Seismogram of traces from 551 to 569 at the interval of 2 recorded from 3:30:22 to 3:42:52 on Oct 29th, 2011

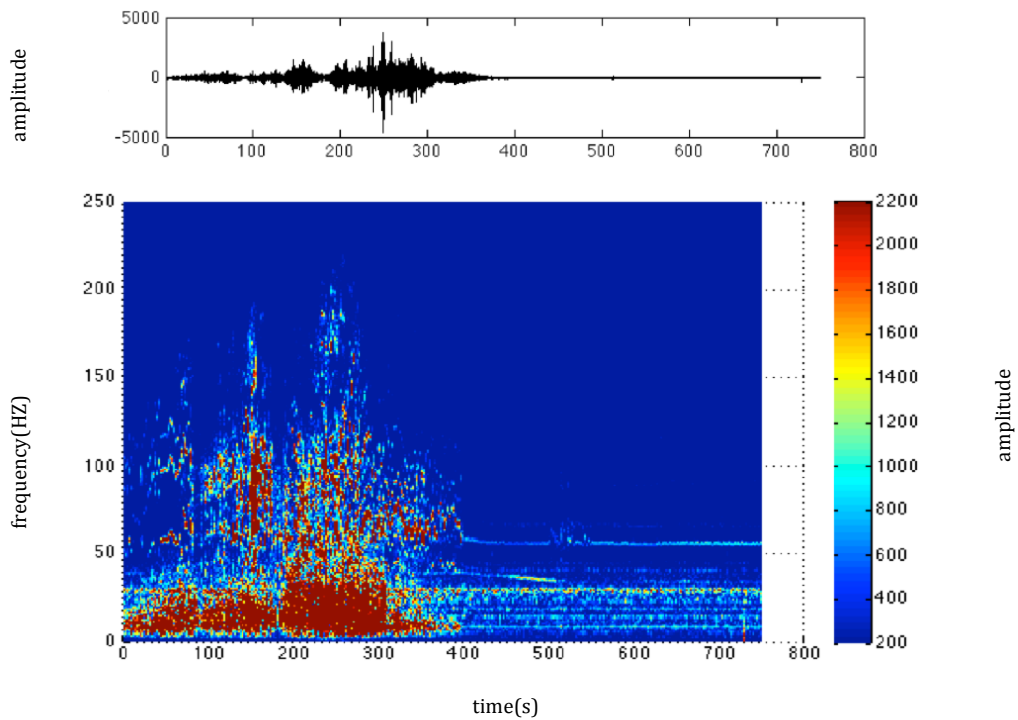


Fig 12. Seismogram and Time frequency representation of trace 590 recorded from 3:43:22 to 3:55:22 on Oct 29th, 2011

Fig 12 is the seismogram of trace 590 recorded from 3:43:22 to 3:55:52 and its time frequency representation. There are 3 events in Fig 12, one is from 0s to 95s the other is from 100s to 180s, the third is from 190s to 300s. They are named as event s4-e4, s4-e5, s4-e6 in the order of time. Fig 13 is the time slice of Fig 12 at 3:47:32 (event s4-e6). Fig 14 is the seismogram of that event from trace 560 to 614 at a trace interval of 6.

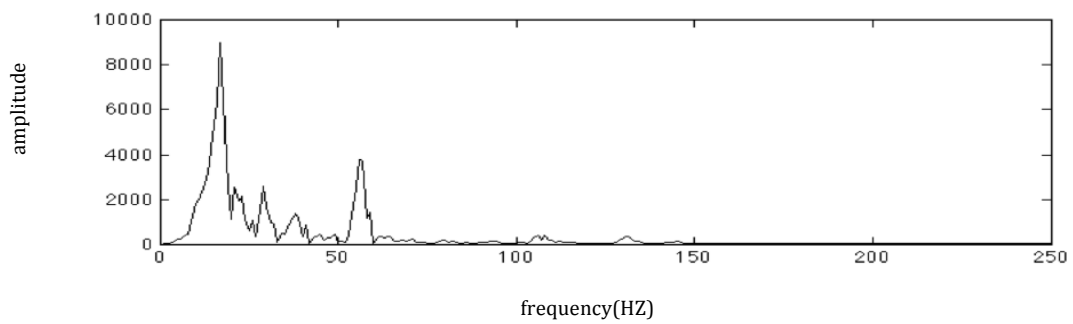


Fig 13. The frequency spectrum of trace 590 of s4-e6 at a selected time

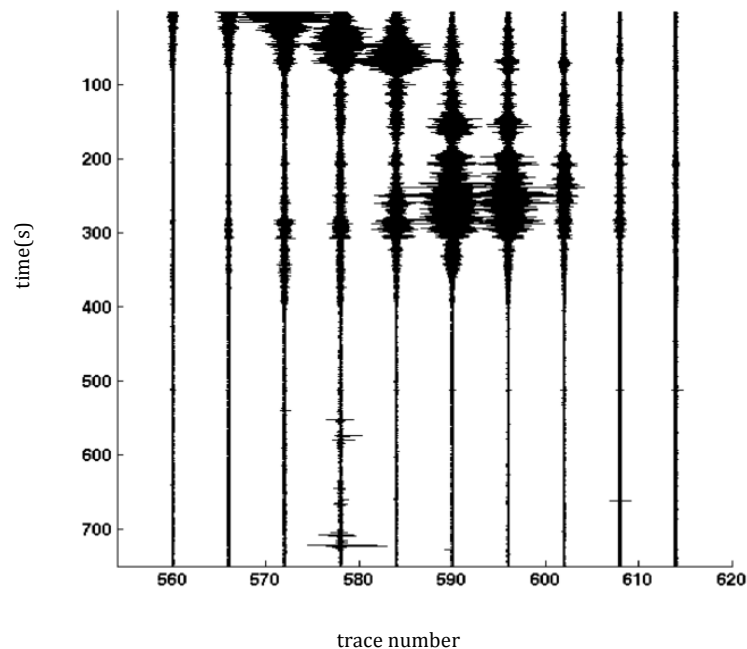


Fig 14. Seismogram of traces from 560 to 614 at the interval of 6 recorded from 3:43:22 to 3:55:52 on Oct 29th, 2011

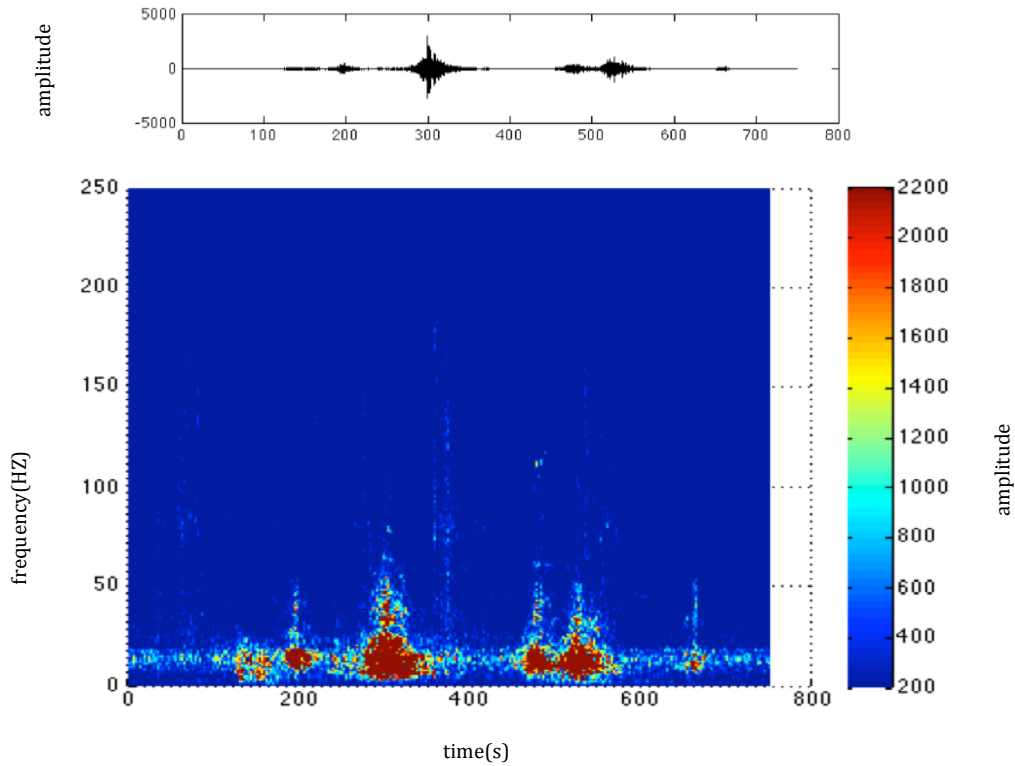


Fig 15. Seismogram and time frequency representation of trace 620 recorded from 3:18:22 to 3:30:52 on Oct 29th, 2011

Fig 15 shows the seismogram recorded from 3:18:22 to 3:30:52. In this figure, I found four events, s4-e7, s4-e8, s4-e9 and s4-e10. Fig 16 is the time slice of Fig 15 at 3:27:32 (event-s4-e10). Fig 17 shows the seismogram of this event from trace 610 to 664 at interval of 6.

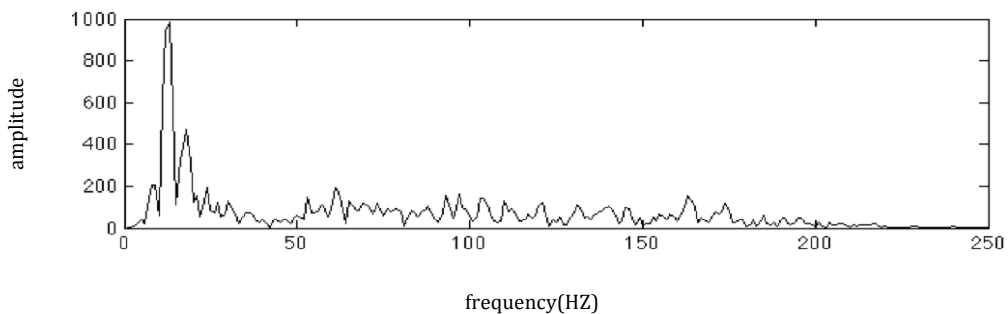


Fig 16. The frequency spectrum of trace 620 of event s4-e10 at a selected time

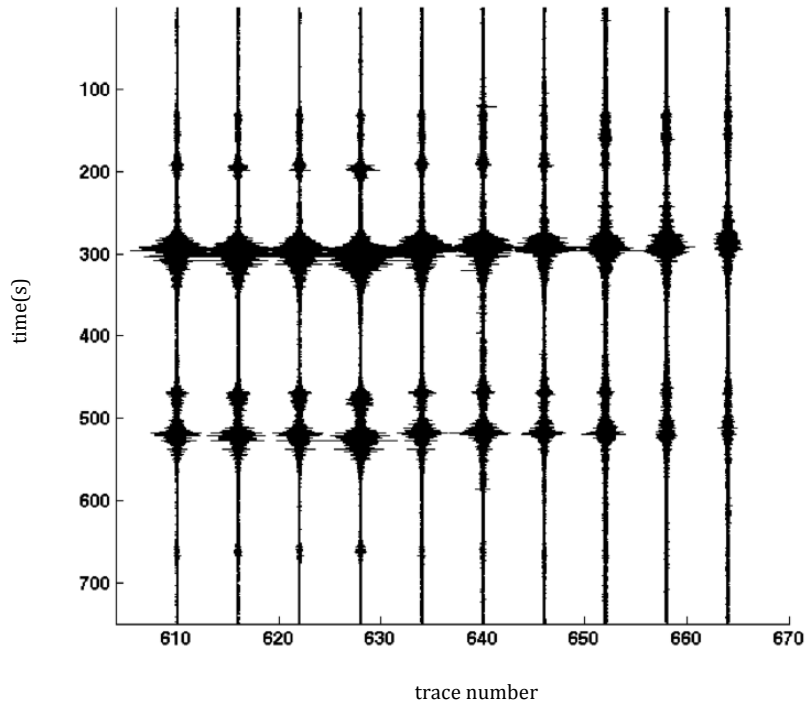


Fig 17. The seismogram of traces from 610 to 664 at the interval of 6 recorded from 3:18:22 to 3:20:52

Fig 18 shows the seismogram and time frequency representation of trace 620 recorded from 16:20:25 to 16:32:55. In this figure, I found one event, s5-e1. Fig 19 is the time slice of Fig 16 at 16:27:35 (event s5-e1), Fig 20 shows the seismogram of that event from trace 610 to 647 at interval of 4.

Fig 21 shows the seismogram and time frequency representation of trace 630 recorded from 17:12:56 to 17:25:26. In this figure, I found two events, s5-e2 (from 200s to 300s) and s5-e3 (from 410s to 510s). Fig 22 and 23 are the time slices of Fig 18 at 17:17:16 (event-s5-e2) and 17:22:06 (event-s5-e3). Fig 24 shows the seismogram of that event from trace 615 to 660 at interval of 5.

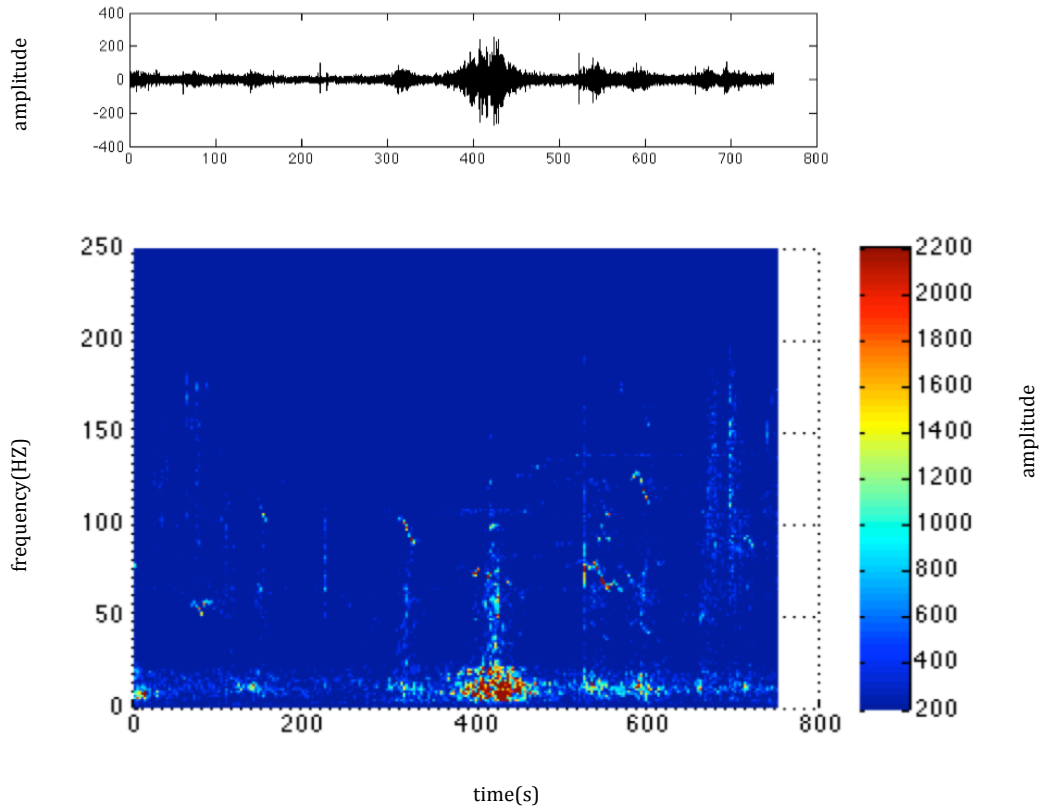


Fig 18. Seismogram and time frequency representation of trace 620 recorded from 16:20:25 to 16:32:55 on Oct 29th, 2011

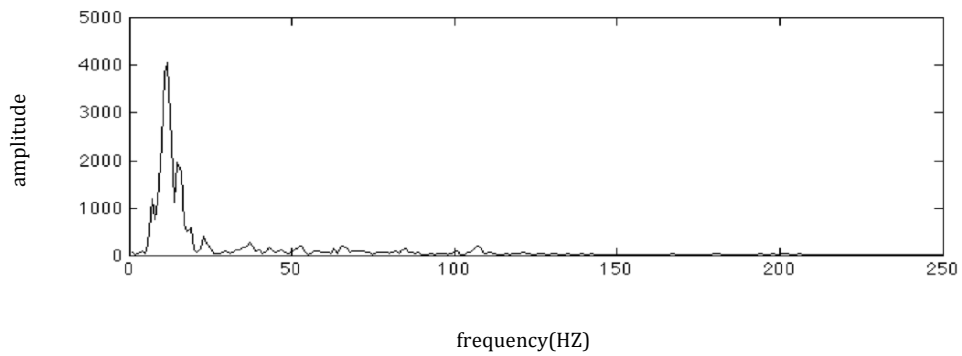


Fig 19. The frequency spectrum of trace 620 of event s5-e1 at a selected time

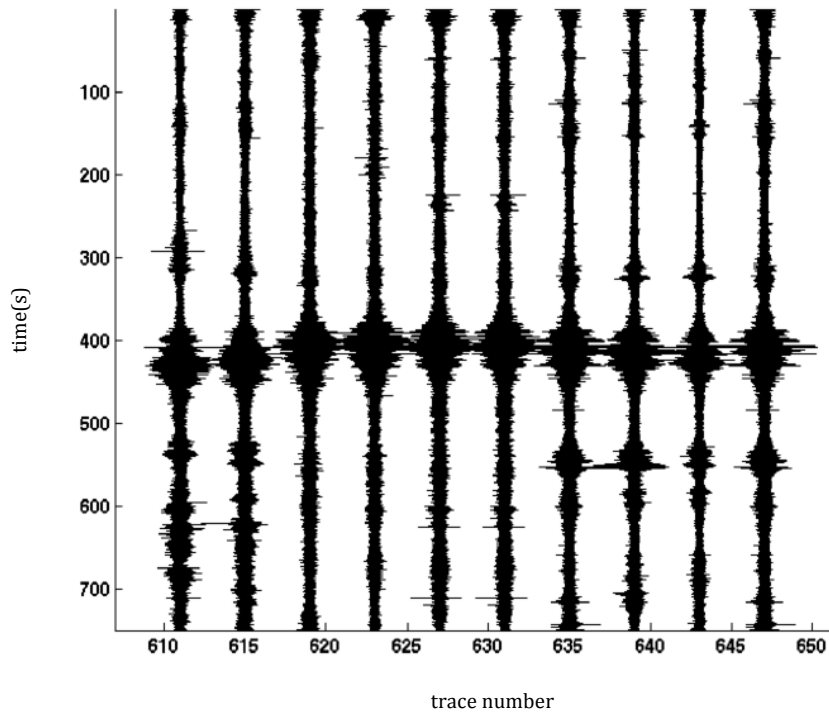


Fig 20. The seismogram of traces from 611 to 647 at the interval of 6 recorded from 16:20:25 to 16:32:55

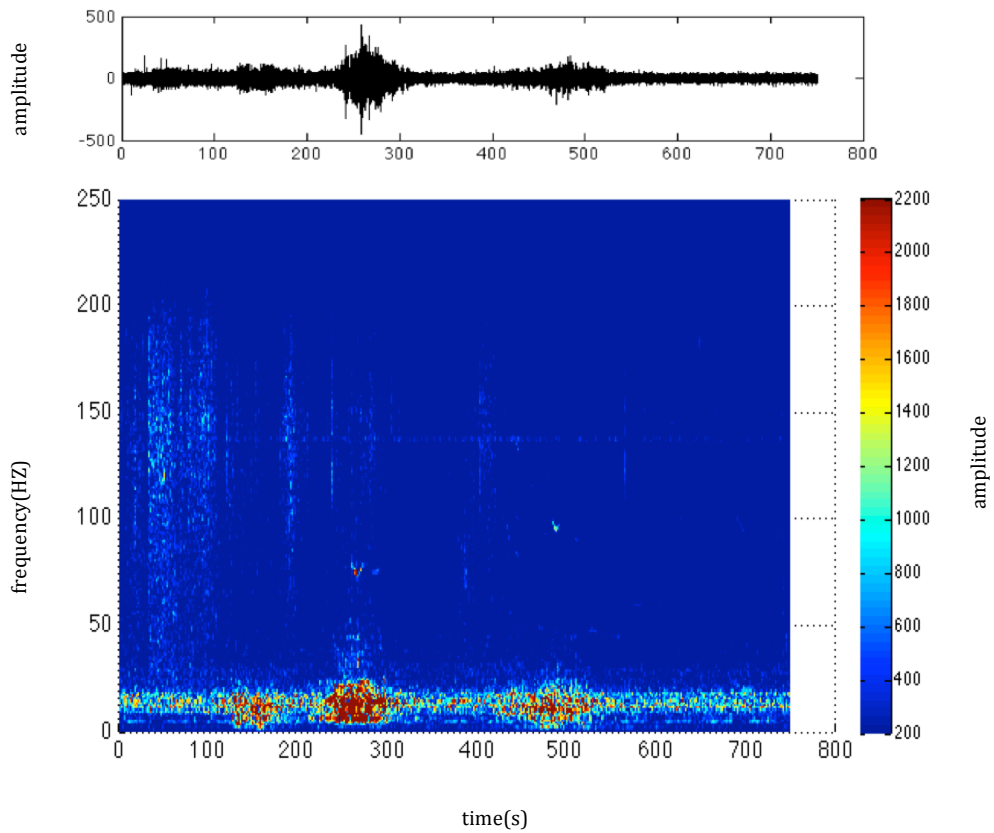


Fig 21. Seismogram and time frequency representation of trace 630 recorded from 17:12:56 to 17:25:26 on Oct 29th, 2011

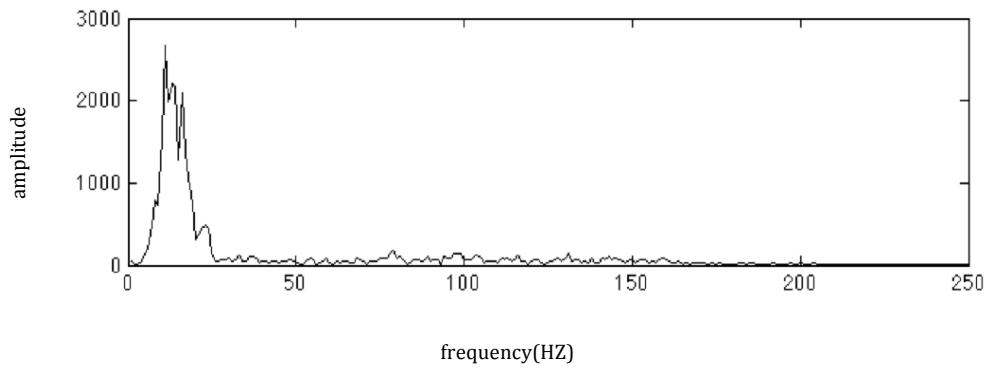


Fig 22. The frequency spectrum of trace 630 of event s5-e1 at a selected time

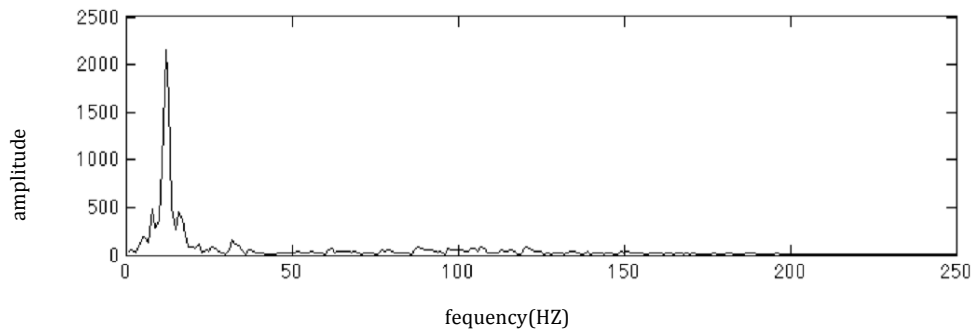


Fig 23. The frequency spectrum of trace 630 of trace s5-e3 at a selected time

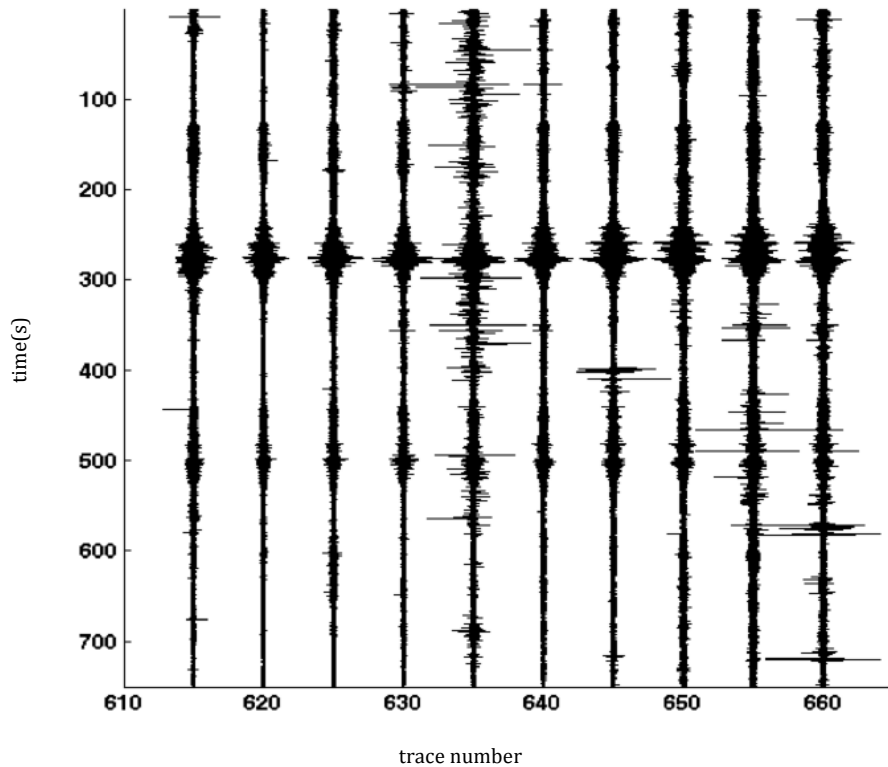


Fig 24. The seismogram of traces from 615 to 660 at the interval of 5 recorded from 17:12:56 to 17:25:26

3.3 Data analysis

For the events I identified, I can categorize them into 2 types. There are 2 major differences for the 2 types of events. The first is their distribution of energy. Fig 25 displays the time frequency representation of 3 traces which contain the LDLF events I identified.

From the T-F representations, we can figure out that for the figures on top, almost all the energy are distributed below 30HZ, while for the 2 figures below, there are still a lot of energy at higher frequency.

Apart from that, the level of energy also shows some difference. Fig 26 shows the frequency spectrum at a given time for 4 LDLF events.

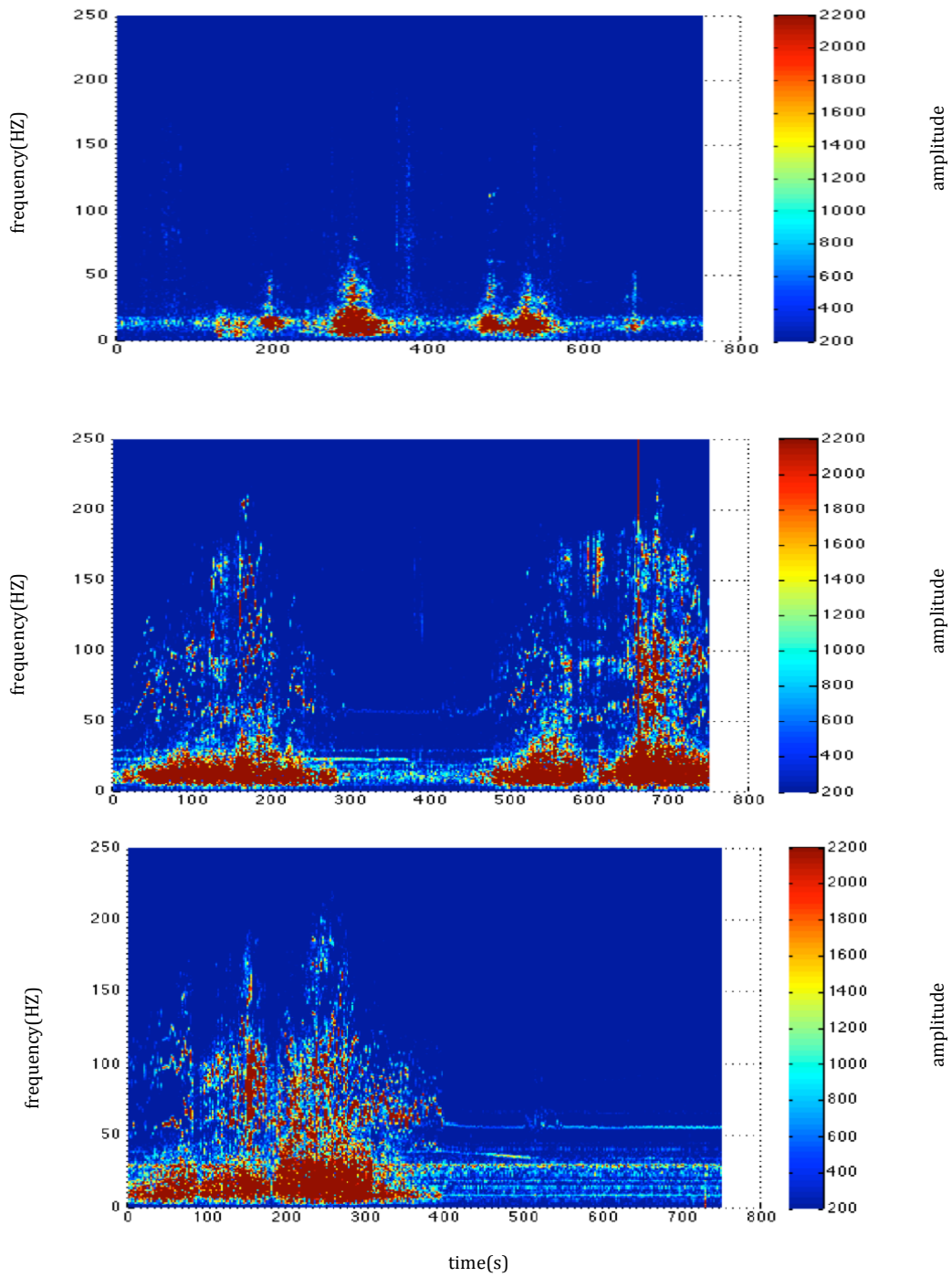


Fig 25. From top to the bottom (a) the T-F representation of trace 620 recorded from 3:18:22 to 3:30:52 (b) the T-F representation of trace 620 recorded from 3:18:22 to 3:30:52 (c) the T-F representation of 564 recorded from 3:30:22 to 3:42:52 (d) the T-F representation of trace 590 recorded from 3:43:22 to 3:55:52

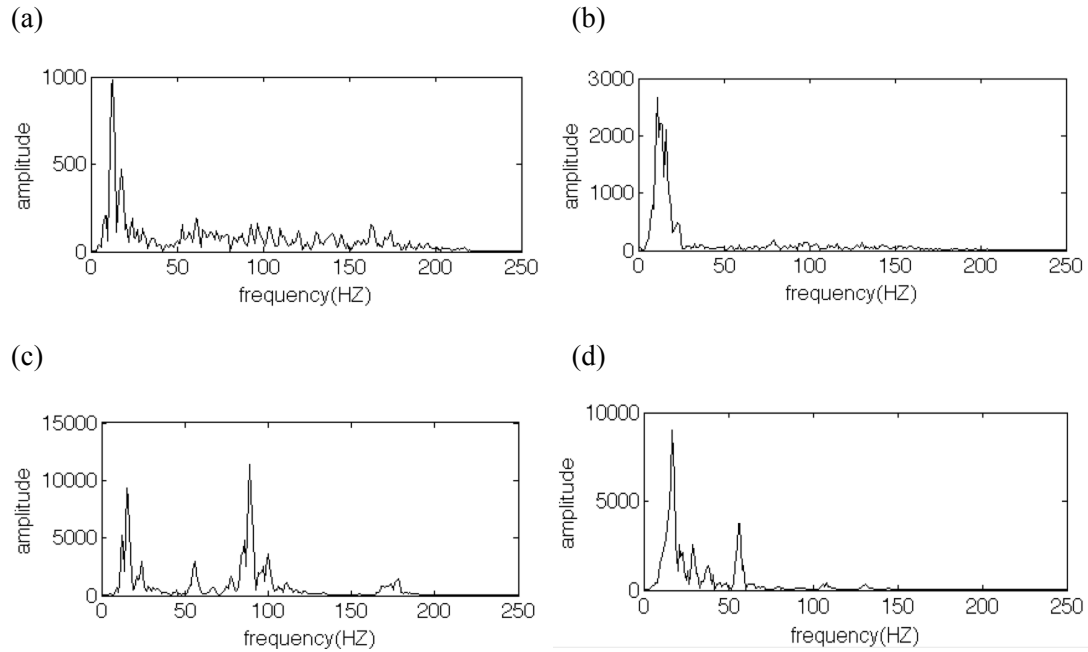


Fig 26. (a)the frequency spectrum of a certain time for event s4-e10 (b) the frequency spectrum of a certain time for event s5-e2 (c) the frequency spectrum of a certain time for event s4-e2 (d) the frequency spectrum of a certain time for event s4-e3

According to the analyses above, the events that have the features of (1) relatively narrow bandwidth (from 5 to 30HZ) and (2) the peak amplitude below 3000 are categorized into type 1 events. The others with multiple energy peaks and larger amplitude are type 2 events. According to these criterias, s4-e7, s4-e8, s4-e9, s4-e10, s5-e1, s5-e2 and s5-e3 are categorized to be type 1 events, and s4-e1, s4-e2, s4-e3, s4-e4, s4-e5 and s4-e6 are categorized to be type 2 events.

3.4 Traveltime picking for the LDLF events

After identifying the LDLF events, we need pick the arrival times of the LDLF signals and use the arrivals to locate the events. Since the duration of the LDLF signals can be up to 200 s, it is difficult to pick the arrivals of each event directly. One LDLF event is probably consisted of many individual events that originate at a similar location but at different times. A reasonable approach is to isolate the long signals to short energy packs and choose the strongest signals to analyze. We have found the dominant frequencies in the LDLF events from the above data processing. They are used to design filters that are applied to the LDLF events. Then, the envelopes of the filtered seismograms are calculated for identifying energy packs. In this research, I choose event s4-e6, s4-e10, s5-e1 and s5-e3 to locate. Among them, s4-e10, s5-e1 and s5-e3 are type 1 events, and s4-e6 is a type 2 event according to the criteria I set previously.

From Fig 16, Fig 19 and Fig 23, we can find out that the dominant frequency for event s4-e10, s5-e1 and s5-e3 are at the frequency of 14HZ, 12HZ, and 10 HZ and there is only one peak for each of the frequency spectrum, so I designed three bandpass filters centered at 14HZ, 12HZ, and 10HZ and apply to the corresponding seismograms respectively and then calculate their envelopes. Fig 27, 28, 29, and 30 show the envelopes after the bandpass filters. For event s4-e3, the frequency spectrum has a different feature compared with the other three events. From Fig 13, it is clear that the spectrum has two peaks, one at around 17HZ the other at around 52HZ, so I design two bandpass filters, one centered at 17HZ the other centered at 52HZ, and apply to the data respectively. The results are shown in Fig 31 and 32. From the

envelopes, we can see more than 1 independent energy packs for the LDLF events. From the envelope, we can find three independent energy packs at around 516s, 527s, and 538s respectively. Table 1(a), 1(b) and 1(c) shows the traveltime difference for the three energy packs. I name them as s4-e10-p1, s4-e10-p2, and s4-e10-p3 respectively.

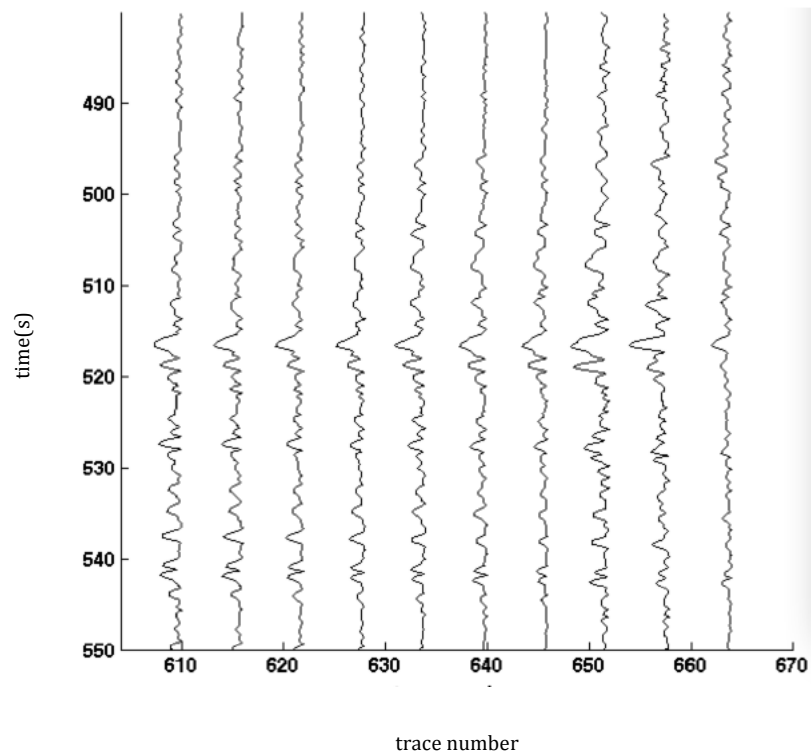


Fig 27. The envelope of event s4-e10 after a band-pass filter centered at 14HZ

The main receivers I used for locating the events were deployed along line 7, but for event s4-e10, I also found they were recorded by receivers from other lines. I pick two receivers (Receiver 375 and 380) off line 7 to locate the events. Fig 28 shows the envelope of event s4-e10 after a bandpass filter centered at 14HZ.

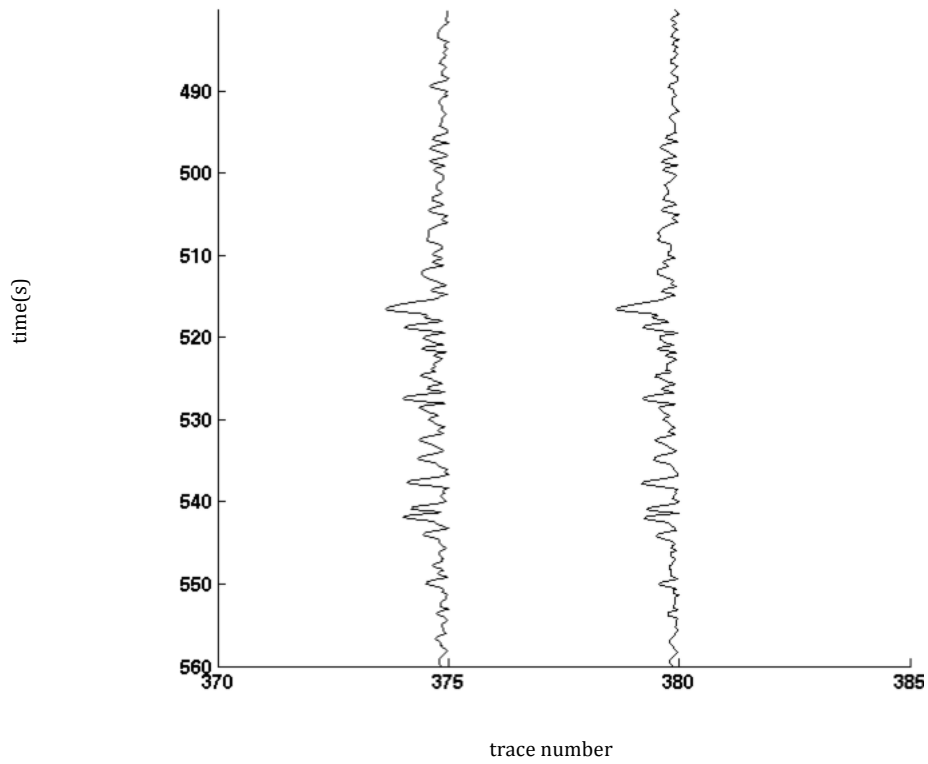


Fig 28. The envelope of trace 375 and 380 of event s4-e10 after a bandpass filter centered at 14HZ

Trace number	Time difference (s)
610	0
616	-0.012
622	-0.020
628	-0.024
634	-0.024
640	-0.020
646	-0.012
652	0.002
658	0.016
664	0.036
375	0.024
380	0.012

Table 1(a). the travelttime difference between trace 610 and other selected traces for energy pack s4-e10-p1

Trace number	Time difference (s)
610	0
616	-0.012
622	-0.022
628	-0.026
634	-0.028
640	-0.024
646	-0.016
652	-0.006
658	0.008
664	0.026
375	0.032
380	0.022

Table 1(b). the travelttime difference between trace 610 and other selected traces for energy pack s4-e10-p2

Trace number	Time difference (s)
610	0
616	-0.012
622	-0.022
628	-0.028
634	-0.028
640	-0.026
646	-0.02
652	-0.01
658	0.004
664	0.022
375	0.014
380	0.006

Table 1(c). the travelttime difference between trace 610 and other selected traces for energy pack s4-e10-p3

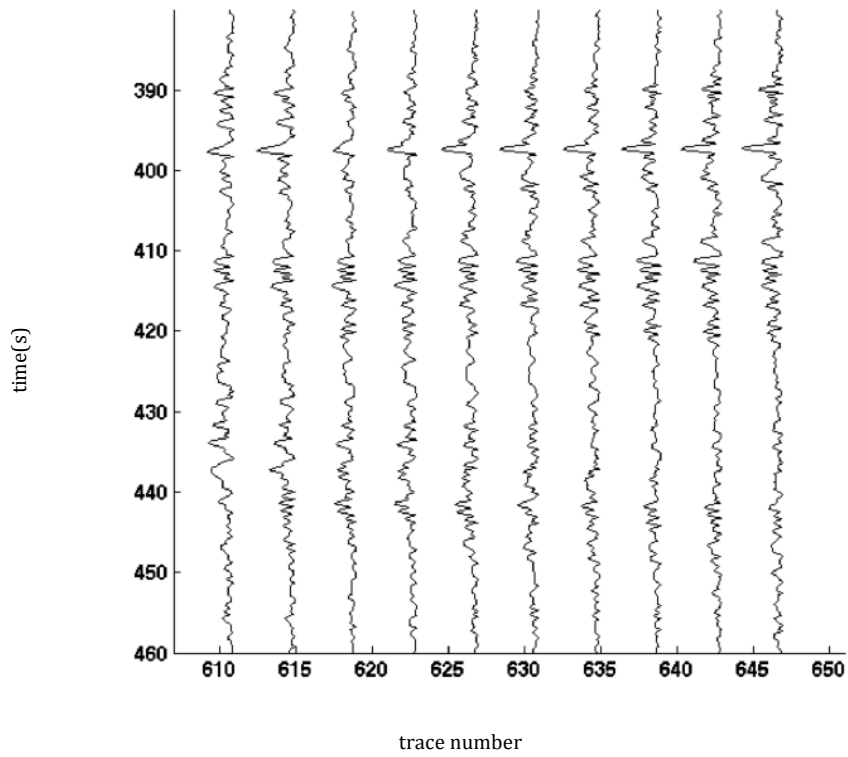


Fig 29. The envelope of event s5-e1 after a bandpass filter centered at 12HZ

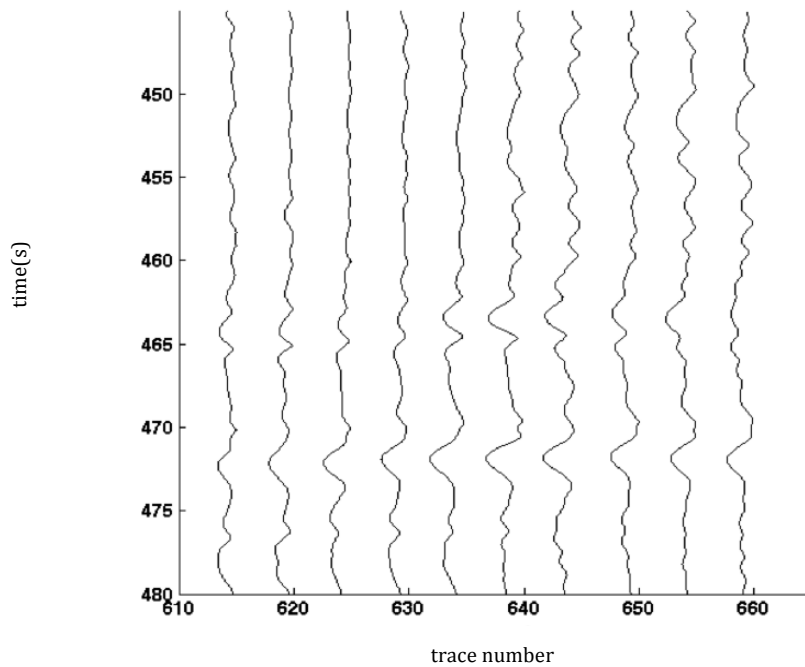


Fig 30. The envelope of event s5-e3 after a bandpass filter centered at 10HZ

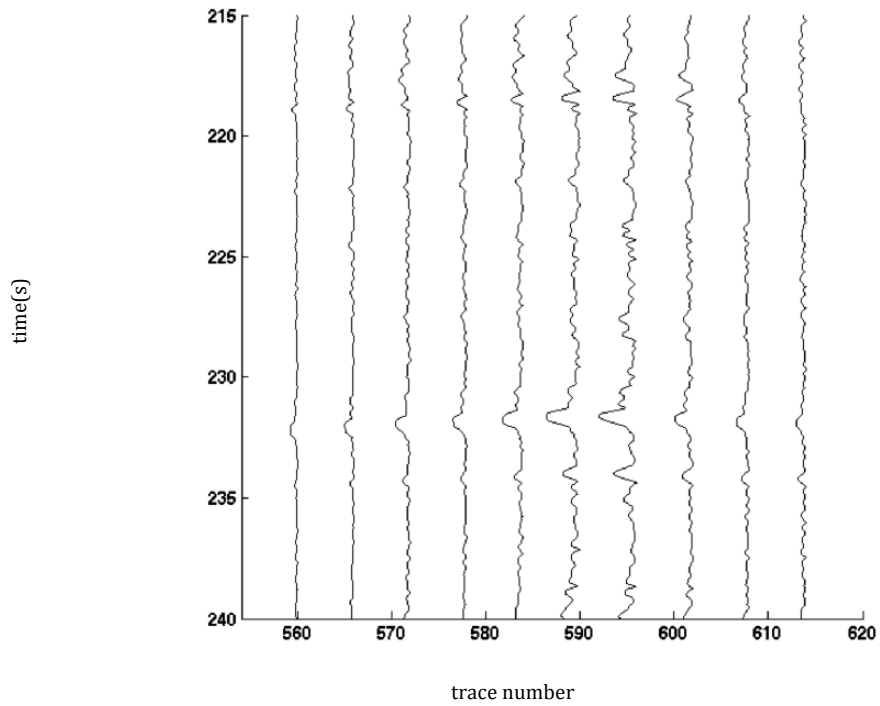


Fig 31. Envelope of traces from 560 to 614 at the interval of 6 recorded from 3:46:02 to 3:48:22 on Oct 29th, 2011 after a filter centered at 17HZ

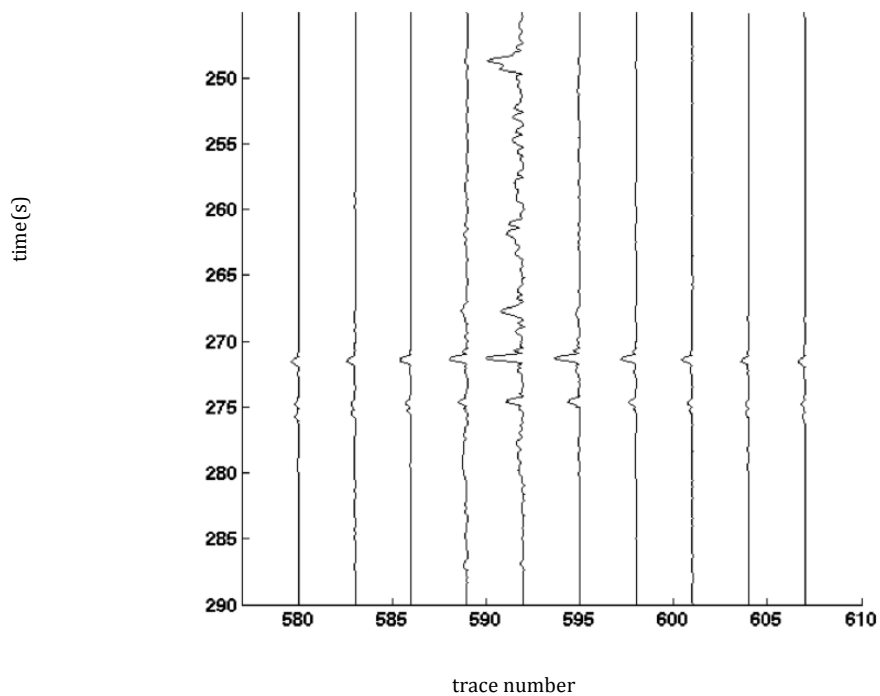


Fig 32. Envelope of traces from 580 to 607 at the interval of 3 recorded from 3:46:02 to 3:48:22 on Oct 29th, 2011 after a filter centered at 52HZ

From the envelope, we can find two groups of independent energy packs at around 390s and 398s respectively. Table 2 shows the travelttime difference for the two energy packs. I name them as s5-e1-p1 and s5-e1-p2 respectively.

(a)

Trace number	Time difference(s)
611	0
615	-0.024
619	-0.046
623	-0.062
627	-0.074
631	-0.08
635	-0.084
639	-0.082
643	-0.076
647	-0.066

(b)

Trace number	Time difference(s)
611	0
615	-0.026
619	-0.048
623	-0.066
627	-0.08
631	-0.088
635	-0.094
639	-0.094
643	-0.09
647	-0.08

Table 2. the travelttime difference between trace 611 and other selected traces for event s5-e1.(a)s5-e1-p1(b)s5-e1-p2

From the envelope, we can find two independent energy packs at around 464s and 472s respectively. Table 3 shows the traveltime difference for the two energy packs. I name them as s5-e3-p1 and s5-e3-p2 respectively.

(a)

Trace number	Time difference(s)
615	0
620	-0.014
625	-0.024
630	-0.030
635	-0.032
640	-0.032
645	-0.026
650	-0.016
655	-0.002
660	-0.014

(a)

Trace number	Time difference(s)
615	0
620	-0.014
625	-0.024
630	-0.032
635	-0.034
640	-0.034
645	-0.028
650	-0.020
655	-0.006
660	-0.010

Table 3. the traveltime difference between trace 615 and other selected traces for event s5-e3 (a) s5-e3-p1(b)s5-e3-p2

Trace number	Time difference(s)
560	0
566	-0.118
572	-0.238
578	-0.358
584	-0.478
590	-0.598
596	-0.594
602	-0.474
608	-0.354
614	-0.234

Table 4. the traveltime difference between trace 560 and other selected traces for event s4-e6 after it is filtered by a bandpass filter centered at 17HZ

Trace number	Time difference(s)
560	0
566	-0.062
572	-0.124
578	-0.186
584	-0.246
590	-0.254
596	-0.192
602	-0.132
608	-0.070
614	-0.008

Table 5. the traveltime difference between trace 580 and other selected traces for event s4-e6 after it is filtered by a bandpass filter centered at 52HZ

Notice that event s4-e3 is the only type 2 event according to the previous criteria. It is also the only event which has two peaks in frequency spectrum. From the envelope after the bandpass filter, the move-out from event s4-e3 is different from other events as well. Fig 33 shows more detail of Fig 31. From this figure, we can read that the apparent velocity for this event is 1000m/s. Moveout analysis also shows that when event s4-e6 is filtered by a bandpass filter centered at 52HZ, the apparent velocity is 1040m/s.

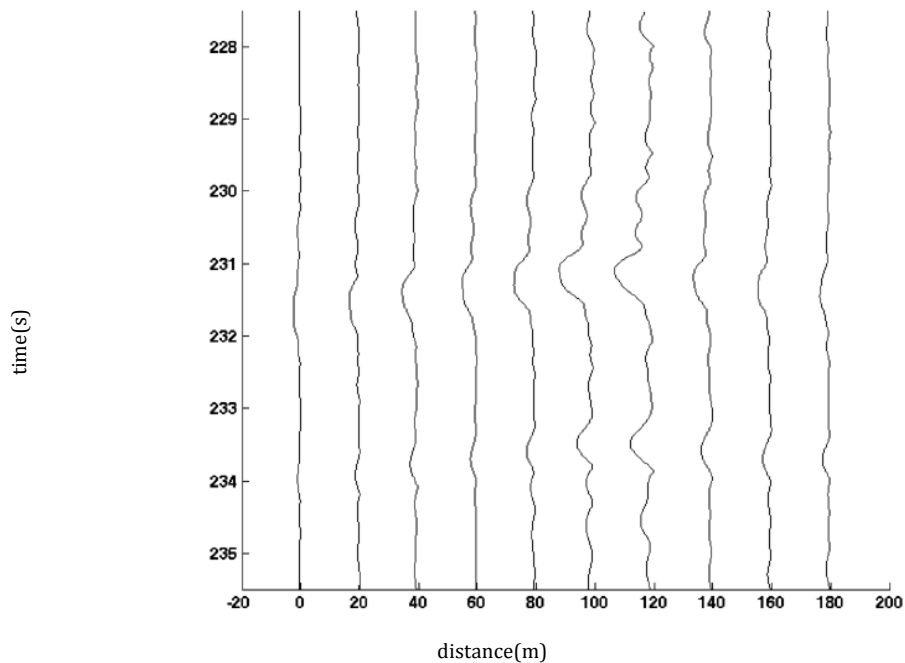


Fig 33. The envelope of event s4-e6 after a bandpass filter centered at 17HZ

Chapter 4. Locating the LDLF events by grid search method

4.1 The grid search method

The grid search method divides the formation into tens of thousands of grids and takes the center of each grid as the potential hypocenter location. A velocity model is needed for calculate traveltimes. Well logs or perforation shots are used to construct and calibrate the velocity model. Then the traveltimes at all receivers from each grid can be calculated after ray tracing through the velocity model. After calculating the traveltimes from all the grids, we can compare the misfit between the observed traveltimes and the calculated traveltimes. The minimum L2 norm is used as the standard to measure the misfit. To speed up the calculation, we first use large grids and find out which grid has the minimum misfit, then divide this specific grid into smaller sub grids to redo the search. This step is repeated several times till the change of the minimum misfit is small enough for accuracy.

4.2 Velocity model and geometry

In the study area, the velocity model is relatively simple. A uniform P-wave velocity of 2800m/s was used by the company Pemex to locate conventional microseismic events. The model was based on well logs. We also use this velocity model for locating the type 1 (s4-e10, s5-e1 and s5-e3) LDLF events. In terms of the type 2 events, the observation shows that its apparent velocity is around 1000m/s. Assuming P- and S-wave ratio is 2.5 in this area, S-wave velocity is about 1120m/s.

Rayleigh wave velocity in this area is about 1040m/s based on the empirical relationship of $0.92 V_s$. We therefore believe that observed phases for this event are Rayleigh wave and use the measured apparent velocities to locate the event, 1000m/s for event s4-e6 after a bandpass filter centered at 17HZ and 1040m/s for event s4-e6 after a bandpass filter centered at 52HZ.

We treat the coordinate of receiver 679 as the origin of the coordinate system. In this case, all the receivers are located within the area of 1776 to 2218 m in x and -3363 to -1544 m in y. The model ranges from -1600 to 2400 m in x axis, -3600 to 2000 m in y, and 0 to 2000 m in z . The large grid size for the first searching has a dimension of 48m*48m*48m and the small grid has the dimension of 3m*3m*3m. In the process of locating, we first calculated the traveltimes of the large grids one by one and found out the minimum misfit in terms of traveltime difference between the observed and calculated values. Then within that large cube which has the minimum traveltime, we calculate the traveltime difference by the small grid and also found out the one that has the smallest misfit in terms of traveltime difference.

4.3 Locating results

The locations of the LDLF events are shown in Fig. 34 (map view) and Fig. 35 (sectional view). Fig 36 shows the locations of type 1 events in a 3D view, on which , the relationship between the source locations and the location of the well can be more clearly viewed. Type 1 events are located almost at the same depth with the horizontal well. The events recorded in stage 4 and 5 are located around the treatment area of stage 4 and 5, respectively. A very interesting phenomenon is that the earlier energy

pack is closer to the horizontal well than the later ones, suggesting that the sources migrate away from the horizontal well with time. These events are probably caused by fluid pressurization in fractures.

For type 2 events, they are located near the surface, far above the treatment well. Their relation with the hydraulic fracturing process is not clear. Type 2 events may be caused by the vibration of equipment at the surface.

event	s4-e10-p1	s4-e10-p2	s4-e10-p3	s5-e1-p1	s5-e1-p2
X(m)	306	339	372	285	327
Y(m)	-1008	-969	-937	-899	-846
Z(m)	1464	1497	1524	1515	1503

event	s5-e2-p1	s5-e2-p2	s4-e6-p(17)	s4-e6-p(52)
X(m)	309	324	756	768
Y(m)	-919	-892	-1671	-1683
Z(m)	1485	1497	36	27

Table 6a. The locations for each energy pack

event	s4-e10-p1	s4-e10-p2	s4-e10-p3
X(m)	303	333	363
Y(m)	-1008	-960	-928
Z(m)	1467	1497	1524

Table 6b. The locations for the energy packs from event s4-e10 if only using receivers in line 7 for locating

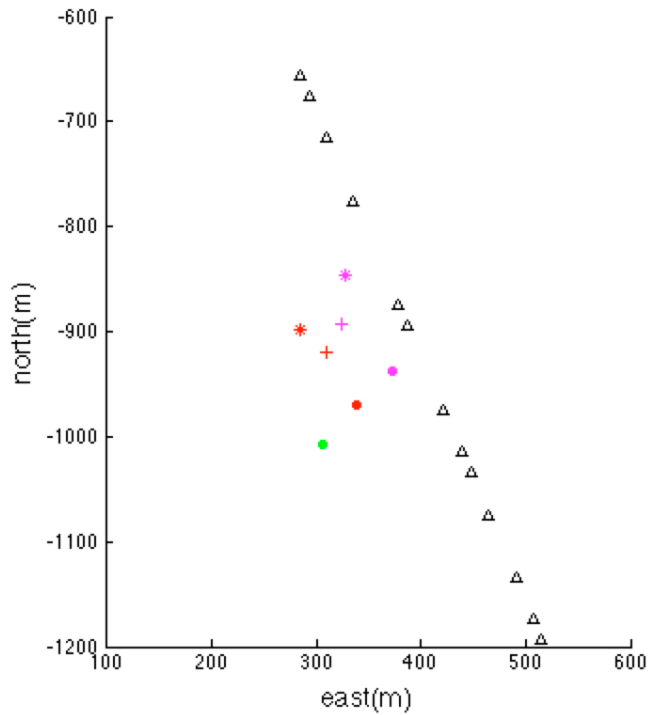


Fig 34. Source locations of the LDLF events in a map view. Open triangles are stations. Blue dots are for type 2 events. Other colored symbols are the locations of 3 type 1 events. One symbol is for one event. Pink indicates the sources are from the earliest signals, red from later signals, and green from the latest.

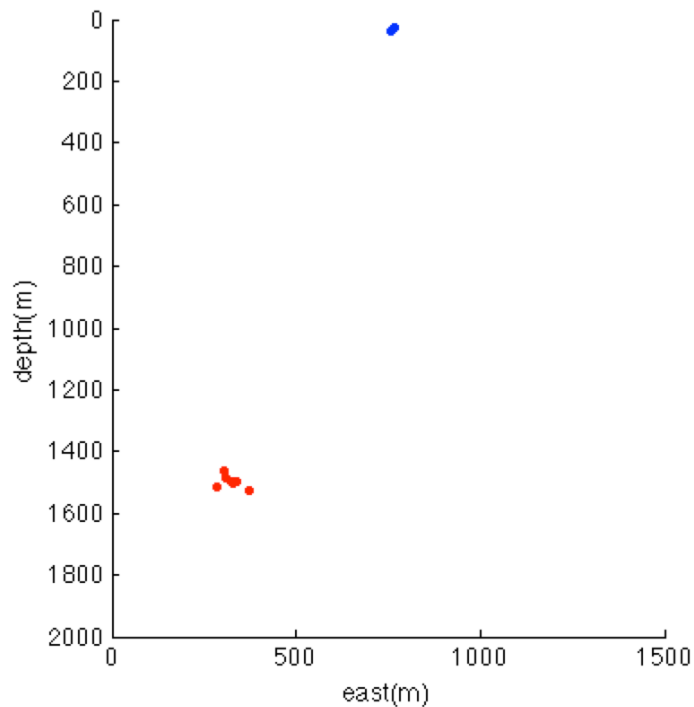


Fig 35. Sectional view of the source locations. All type 1 events are represented by red dots and type 2 events are blue dots

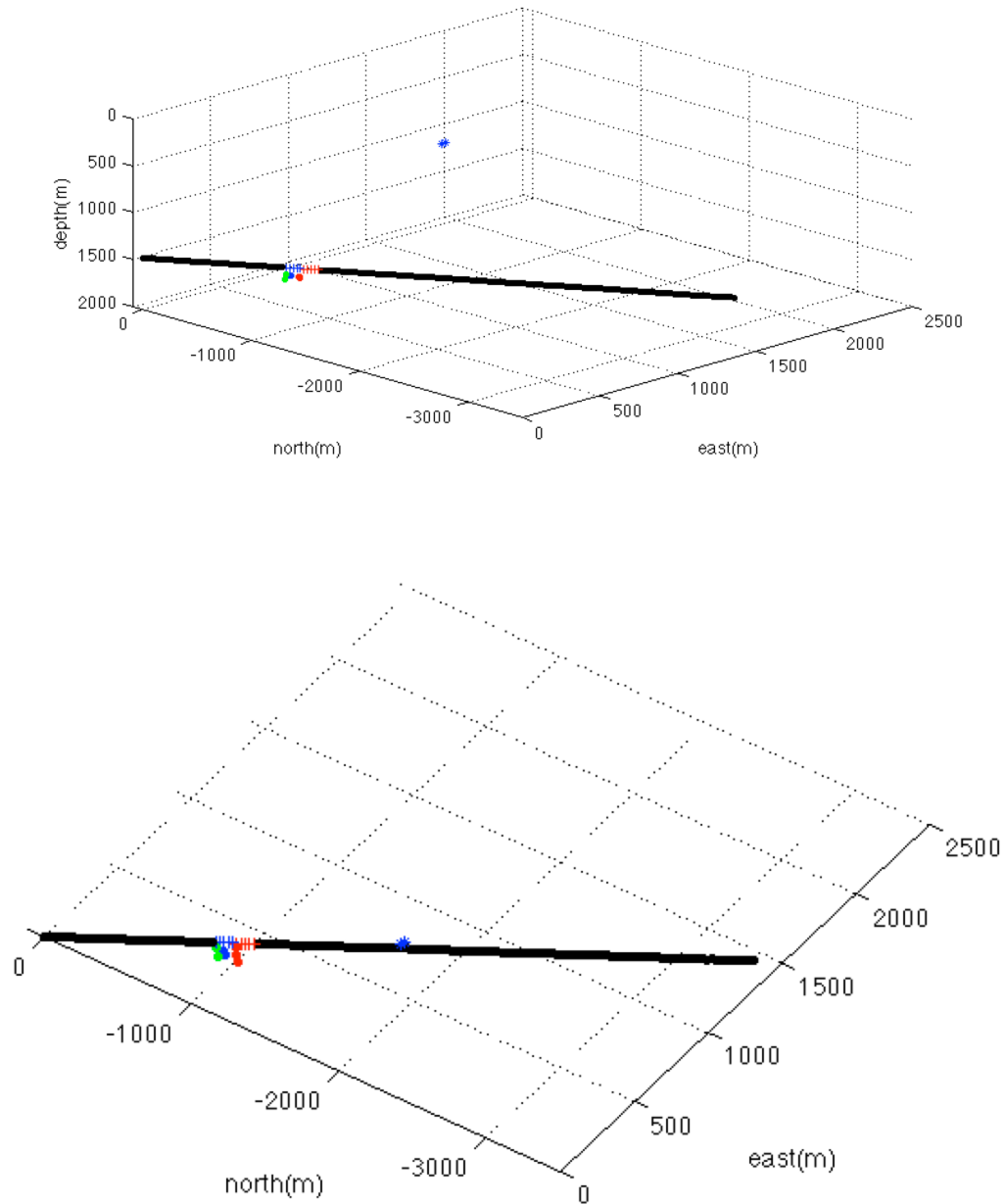


Fig 36. The figure on top is the 3D detailed view of the source locations. The figure below is the map view of the source locations. The red '+' is the location of stage 4, the blue '+' is the location of stage 5. The red dots represent the locations of sources from events recorded during stage 4, the blue and green dots represent the locations of sources from events recorded during stage 5, the black line is other parts of the horizontal well

4.4 Error estimation of the locations

The accuracy of event location depends on the quality of data, the method, and the velocity model. To estimate possible errors in the event locations, we conduct tests on errors caused by the method and by errors in the data. We do not estimate the errors due to inaccurate velocity as the uncertainties in velocity often causes systematic errors in all events.

First, we want to test if the L2 norm at the location is distinguishable from those at the surrounding grid points. We calculate the L2 norms at source location (306, -1008, 1464) and its surrounding grids and plot the results in Fig 37 for energy pack s4-e10-p1. The result shows that the L2 norm at the source location is significantly smaller than those at its surrounding grids in all three directions. The misfit is more sensitive along x- and y- directions. This is due to that all receives are much widely distributed in x and y than in z direction. The grid search method can accurately determine the minimum misfit for the source location. The location error caused by the method is the minimum grid size in this case. Fig 38 displays the errors in the case that energy packs were only located by receivers deployed along line 7. By comparing fig 37 with fig 38, we can find out that by adding two receivers off line 7, the traveltimes error increase more rapidly when the grids is moving away from the source locations in terms of x- and y- direction. But the change in z- direction is not so apparent.

Secondly, we estimate the source location error caused by errors in the traveltimes. Assuming a phase picking error of 0.002s (one sampling point), we make all the traveltimes longer or shorter by 2 standard errors (0.004s) for event s4-e10-p1

and relocate the event. For the situation that the traveltime difference is 0.004s faster, the location from data with adding errors differ from the original one are 9m in x, 12 m in y, and -6m in z; If the traveltime difference is 0.004s slower, The location from data with adding errors differ from the original one are -12m in x, -9 m in y, and 6m in z. The results are shown in Table 8 and Figure 39. This experiment reveals that the location error due to the traveltime picking error in the data is larger than that due to the limitation of the grid size. We then choose up limit 12m as the possible errors in the event locations.

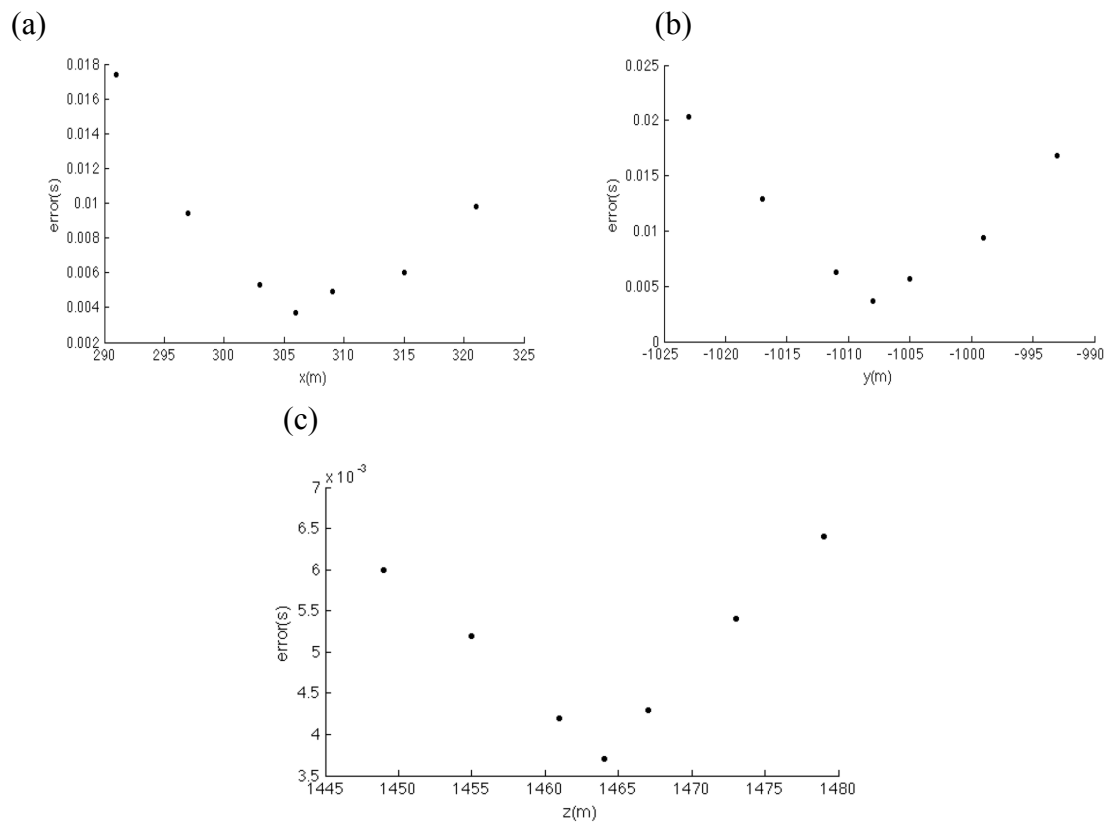


Fig 37. Distance versus errors for grids surrounded the source location (306, -1008, 1464) (a) the horizontal axis represents the x- coordinate of the grids, y- and z- coordinates of the grids are -1008, 1464 (b) the horizontal axis represents the y- coordinate of the grids, x- and z- coordinates of the grids are 306, 1464 (c) the horizontal axis represents the z- coordinate of the grids, x- and y- coordinates of the grids are -306, -1008

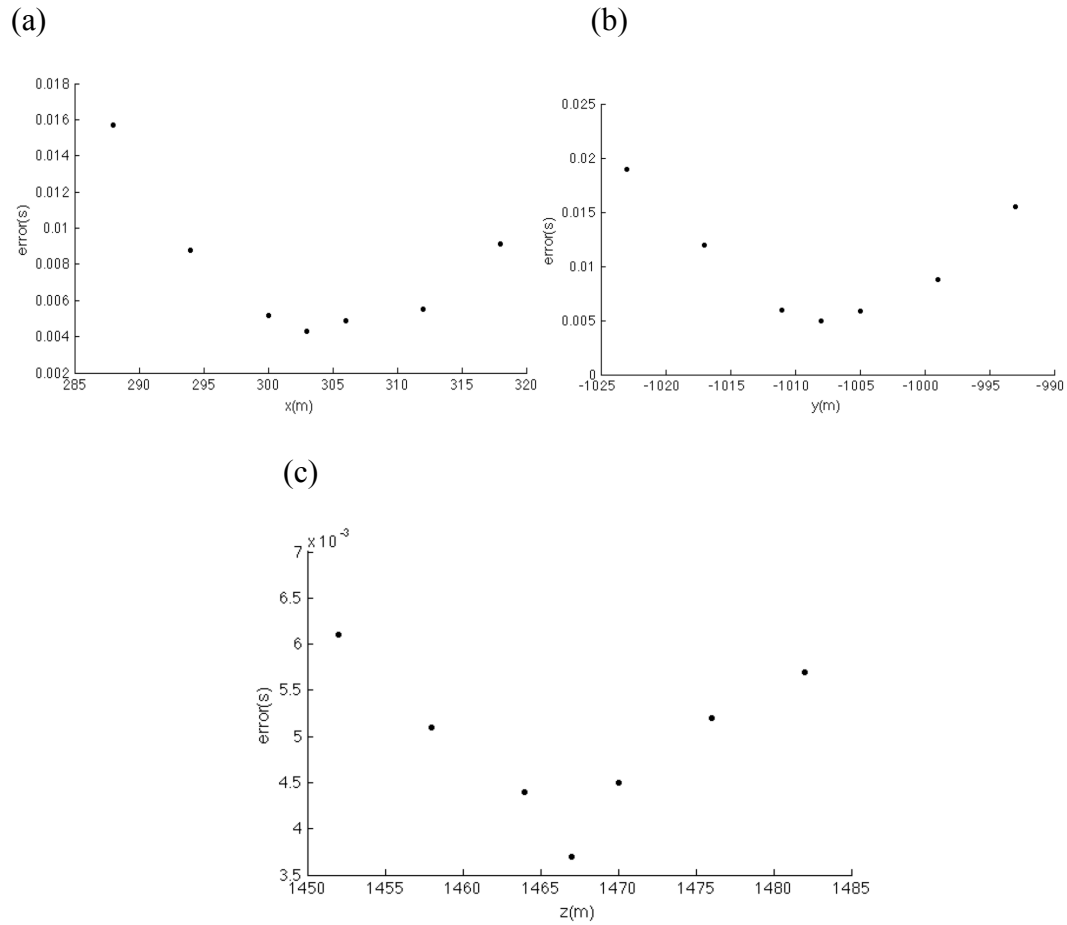


Fig 38. Distance versus errors for grids surrounded the source location (303, -1008, 1467) (a) the horizontal axis represents the x- coordinate of the grids, y- and z- coordinates of the grids are -1008, 1467 (b) the horizontal axis represents the y- coordinate of the grids, x- and z- coordinates of the grids are 303, 1467 (c) the horizontal axis represents the z- coordinate of the grids, x- and y- coordinates of the grids are 303, -1008

(a)

Trace number	Time difference(s)
610	0
616	-0.016
622	-0.024
628	-0.028
634	-0.028
640	-0.024
646	-0.016
652	0.006
658	0.020
664	-0.234
375	0.040
380	0.028

(b)

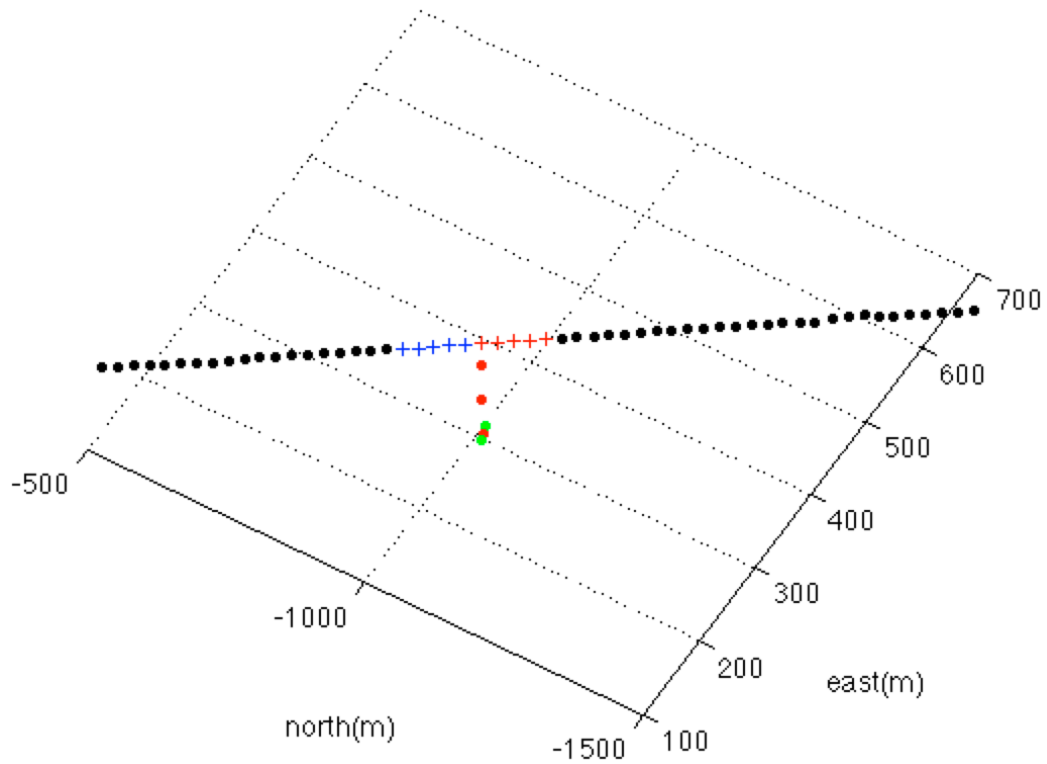
Trace number	Time difference(s)
610	0
616	-0.008
622	-0.016
628	-0.020
634	-0.020
640	-0.016
646	-0.008
652	-0.002
658	0.012
664	0.032
375	0.020
380	0.008

Table 7. the travelttime difference between trace 610 and other selected traces for energy pack s4-e10-p1 (a) travelttime differences are 0.004s longer (b) travelttime differences are 0.004s shorter

event	s4-e10-p1(traveltime 0.004s longer)	s4-e10-p1(traveltime 0.004s shorter)
X(m)	315	294
Y(m)	-996	-1017
Z(m)	1458	1470

Table 8. The locations of s4-e10-p1 when the traveltime differences are picked 0.004s longer and shorter

(a)



(b)

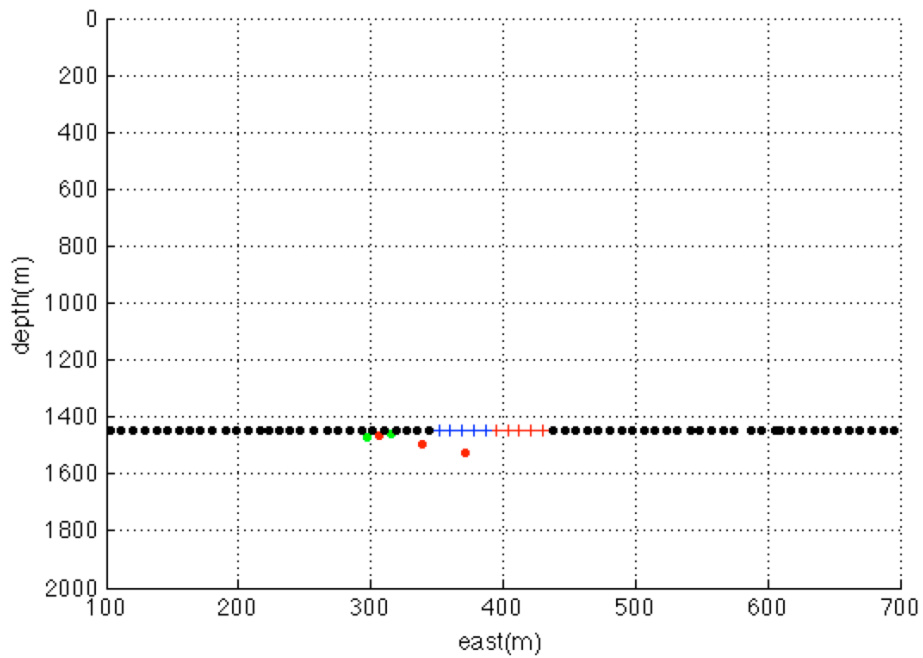


Fig 39. The red dots are the locations of s4-e10-p1, s4-e10-p2 and s4-e10-p3. The green dots are the locations traveltime differences were 0.002s longer or shorter than the picked traveltime differences. (a) map view (b) sectional view

Chapter 5. Discussion

The drilling survey indicates that the depth of the treatment well reaches 1500m as the inclination remains stable around 90 degree. The hypocenters of the 7 energy packs for the 3 type 1 events are 1515m, 1503m, 1485m, 1497m 1524m, 1497m, and 1467m, respectively, close to the depth of the horizontal well in vertical direction. Moreover, the epicenters of these energy packs correlate well with the locations of the treatment stages. Type 1 events are found in both stage 4 and 5 and are probably common type associated with fracturing. The sources seem to migrate away from the treatment well with time, probably indicating the path of fluid flow. We interpret that type 1 events are caused by fluid pressurization when injected fluid flows through the fractures. These events can be potentially useful to map the fracture geometry.

Unlike type 1 events that occurred at the depths close to the horizontal well, the depth of type 2 events is much shallower ($< 50\text{m}$). Amplitude analysis also indicates the locating results from traveltimes are robust. For example, for the events recorded from 03:39:42 to 03:39:52 on Oct 29th, 2011, the maximum amplitude is recorded at receiver 593 (Fig. 40), about 45m away from the hypocenter, which is the shortest distance among all the receivers. This phenomenon is due to that attenuation near the surface is usually strong and causes amplitude decreases significantly with increasing distance. The shallow source depth and the strong amplitude variation among the receivers are consistent with the data analysis that the dominant phase recorded is Rayleigh wave. The mechanism for Type 2 events is not clear, but probably by noise or equipment operation.

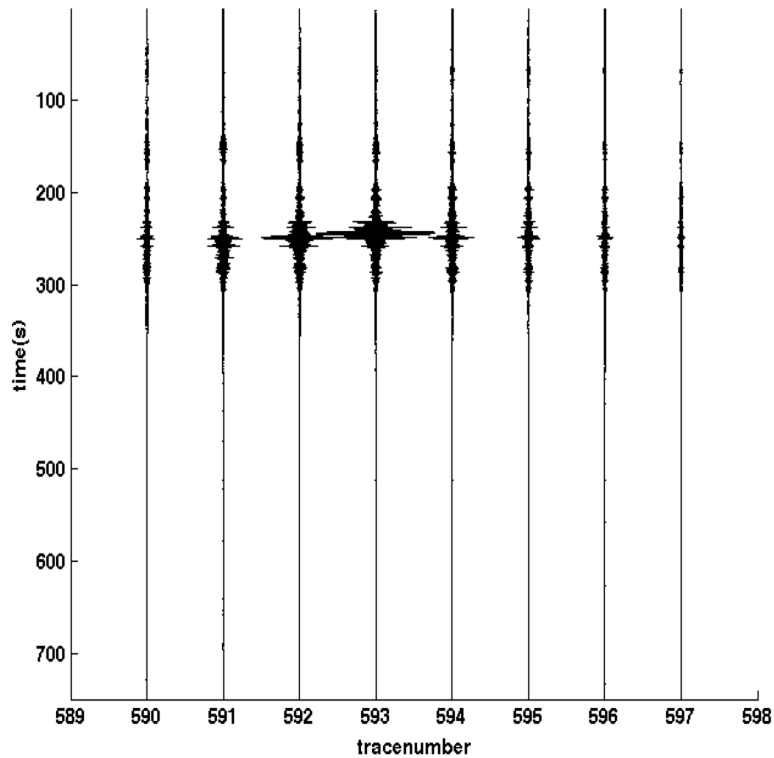


Fig 40. Seismograms from trace 590 to 597 at an interval of 1 recorded from 3:43:22 to 3:55:52.

The amplitude variation with distance for type 1 events is not as obvious as for type 2 events. This is largely due to more vertical ray paths from the deep sources to close surface receivers, which results in a much smaller distance among the receivers. So the energy is attenuated at almost the same amount to each receiver.

Type 1 and 2 events are clearly different in terms of frequency spectrum, energy level, amplitude variation with distance, and moveout velocities from the above data analyses. The location results confirm the difference between the two types by their locations. Type 1 events are common in both stages and are located close to the treatment well at depth, while type 2 events are close to the surface. The locations from energy packs show that the source of type 1 events migrate away from the

treatment well by increasing time, probably indicating fluid flow in fractures. Type 2 events are not common during hydraulic fracturing process and could be caused by some equipment operation.

Chapter 6. Conclusions

We have analyzed seismic data recorded at the surface receivers during hydraulic fracturing in the Montanes shale to study the long-duration low-frequency events. We identified several LDLF events from the data recorded during stage 4 and 5 using frequency-time representations of seismograms. Appropriate band-pass filters were designed and applied to the data to increase the signal-to-noise ratio. The envelopes of filtered data are calculated and used to pick the events traveltimes. Then a grid-search method is used to locate different energy packs for each LDLF event.

The events can be classified into 2 types based on the data and source locations. Type 1 events are commonly present in both stage 4 and 5 with the dominant frequency from 5 to 25 HZ. They are located very close to the treatment well at ~1500m deep and to the places where treatment was performed. Moreover, the sources of such LDLF events tend to migrate away from the treatment well with time. Considering all these observations, we conclude that type 1 events are caused by pressure change related to fluid flow in fractures. The time-dependence source locations could have an important application to characterize the fluid path inside fractures.

Type 2 events have a broad frequency spectrum and are located near the surface. The apparent velocity for the same event depends on frequency, a character of dispersive Rayleigh waves. Type 2 events are only observed at stage 4. It is not completely clear what causes this type of events. One possible explanation is the vibration due to the operation equipment.

Our research indicates that the LDLF events can be triggered by fluid flow in fractures. The source trajectory of these events might be used to characterize fluid paths and the fracture network. More studies from other fracturing experiments are needed to better understand the mechanisms of LDLF events and their usage in mapping fractures.

Bibliography

Aki. K, Fehler, M and Das. S, 1977. Source mechanisms of volcanic tremor: Fluid driven crack models and their application to the 1963 Kilauea eruption, *Journal of Volcanology and Geothermal Research*, 2 (1977) 259-287

Almendros. J, Chouet. B and Dawson. P, 2001. Spatial extent of a hydrothermal system at Kilauea Volcano, Hawaii, determined from array analyses of shallow long-period seismicity 2. Results, *J. Geophys. Res*, 106, 13581-13597

Astakhov. D.K, Roadarmel. W.H and Nanyakkara. A.S, 2012. A new method of characterizing the stimulated reservoir volume using tiltmeter-based surface microdeformation measurements, Paper presented at the SPE Hydraulic Fracturing Technology Conference, The Woodlands, Texas, 6-8 February, Society of Petroleum Engineers, 151017

Bame. D.A, and Fehler .M.C, 1986. Observations of long-period earthquakes accompanying hydraulic fracturing, *Geophys. Res. Lett.*, 13, 149-152

Becken. M, Ritter. O, Bedrosian. P.A and Weckmann. U, 2011. Correlation between deep fluids, tremor and creep along the central San Andreas fault, *Nature*, 480(7375), 87(6), 87-90

Chouet. B, 1988. Resonance of a fluid-driven crack: Radiation properties and implications for the source of long-period vents and harmonic tremor, *J. Geophys. Res*, 93, 4375-4400

Chouet. B, 1996. Long-period volcano seismicity: Its source and use in eruption forecasting, *Nature*, 380, 309-316

Chouet. B, Saccorotti. G, Martini. B, Dawson. P, Luca. G. D, Milana. G, Scarpa. R, 1997. Source and path effects in the wave fields of tremor and explosions at Stromboli Volcano, Italy, *J. Geophys. Res*, 102, 15129-15150

Dragert. H, Wang. K, and James. T.S, 2001. A silent slip event on the deeper Cascadia subduction interface, *Science*, 292(5521), 1525–1528

Das. I, and Zoback. M.D, 2013a. Long-period, long-duration seismic events during hydraulic stimulation of shale and tight-gas reservoirs — Part 1: Waveform characteristics, *Geophys.*, 78(6), 107-118

Das. I, and Zoback. M.D, 2013b. Long-period long-duration seismic events during hydraulic stimulation of shale and tight-gas reservoirs — Part 2: Location and mechanisms, *Geophys.*, 78(6), 97-105

Das. I, and Zoback. M.D, 2012. Microearthquakes Associated with long period, long duration seismic events during stimulation of a shale gas reservoir, Paper presented at SEG Annual meeting, SEG Technical program extended abstract, 2012, doi: <http://dx.doi.org/10.1190/segam2012-1484.1>

Das. I, and Zoback. M.D, 2011. Long-period, long-duration seismic events during hydraulic fracture stimulation of a shale gas reservoir, *Leading Edge*, 30, 778–786

Fletcher, J.B, McGarr. A, 2011. Moments, magnitudes, and radiated energies of non - volcanic tremor near Cholame, CA, from ground motion spectra at UPSAR, *Geophys. Res. Lett.*, 38, L16314, doi:10.1029/2011GL048636

Granberg, A. (Designer). (2010). Hydraulic fracturing of natural gas. [Web Drawing]. Retrieved from <http://www.circleofblue.org/waternews/2010/science-tech/climate/hydraulic-fracturing-infographic/>

Ito, Y, Obara, K, Shiomi, K, Sekine, S, and Hirose, H, 2006. Slow earthquakes coincident with episodic tremors and slow slip events: *Science*, 315, 503–506

Ide, S, Beroza, G.C, Shelly, D.R and Uchida, T, 2007. A scaling law for slow earthquakes, *Nature*, 447, 76-79

Konstantinou, K.I, Schlindwein, V, 2003, *Nature*, wavefield properties and source mechanism of volcanic tremor: A review, *J. Volcanol. Geotherm. Res.*, 119, 161–187

Katsumata, and Kamaya, N, 2003. Low-frequency continuous tremor around the Moho discontinuity away from volcanoes in the southwest Japan, *Geophys. Res. Lett.*, 30(1), 20-1-20-4, doi:10.1029/2002GL0159812

Kieffer, S.W, 1984. Seismicity of Old Faithful Geyser: An isolated source of geothermal noise and possible analogue of volcanic seismicity, *J. Volcanol. Geotherm. Res.*, 22, 59-95

Lesage, P, Mora, M.M, Alvarado, G.E, Pacheco, J, Métaixian, J.P, 2006. Complex behavior and source model of the tremor at Arenal volcano, Costa Rica, *J. Volcanol. Geotherm. Res.* 157 (1–3), 49–59

Maxwell, S.C, Cipolla, C, 2011. What does microseismicity tell us about hydraulic fracturing, Paper presented at SPE Annual Technical Conference and exhibition in Denver, 30 Oct-2 Nov, Society of Petroleum Engineers, 146932, doi: <http://dx.doi.org/10.2118/146932-MS>

M. van der Baan and D.W. Eaton, 2014. Interpretation of resonance frequencies recorded during hydraulic fracturing treatments, *Journal of Geophysical Research: Solid Earth*, 10.1002/2013JB010904

Miller. M.M, Melbourne. T, Johnson. D.J and Sumner. W.Q, 2002. Periodic Slow Earthquakes from the Cascadia Subduction Zone, *Science*, 295, 2423

McNutt. S.R, 1992. Volcanic tremor, in *Encyclopedia of Earth System Science*, vol. 4, p. 417–425

McNutt. S.R, 1996. Seismic monitoring and eruption forecasting of volcanoes: A review of the state-of-the-art and case histories. In: Scarpa, Tilling (Eds.), *Monitoring and Mitigation of Volcanic Hazards*. Springer, Berlin, p. 100-146

Nadeau. R.M, Guilhem. A, 2009. Nonvolcanic tremor evolution and the San Simeon and Parkfield, California, earthquakes, *Science*, 325, 191–193

Ogiso. M, Yomogida. K, 2012. Migration of tremor locations before the 2008 eruption of Meakandake Volcano, Hokkaido, Japan, *J. Volcanol. Geotherm. Res*, 217-218, 8-20

Richardson. J.P, Waite. G.P, 2013. Waveform inversion of shallow repetitive long period events at Villarrica Volcano, Chile, *J. Geophys. Res, Solid earth*, 118, 4922-4936

Shelly .D.R, and Beroza .G.Cand S. Ide, 2007. Complex evolution of transient slip derived from precise tremor locations in western Shikoku, Japan, *Geochemistry Geophysics Geosystems*, 8, Q10014

Shelly. D.R, 2009. Possible deep fault slip preceding the 2004 Parkfield earthquake, inferred from detailed observations of tectonic tremor, *Geophys. Res. Lett.*, 36, L17318, doi:10.1029/2009GL039589

Torres. R.Z, Castagna. J.P, Chesnokov. E.M, and Li. A, 2014. Integration of 2D seismic, Surface microseismic, VSP and well logs: Eagle Ford Shale, Mexico, PHD Dissertation, University of Houston

Walser. D.W, Roadarmel. W.H, 2012. Integrating Microseismic with Surface Microdeformation Monitoring to Characterize Induced Fractures in the Immature Eagle Ford Shale, Paper ARMA 12-594 presented at the 46th U.S. Rock Mechanics/Geomechanics Symposium, Chicago, Illinois, 24–27 June

Warpinski. N.R, Mayerhofer. M.J, Agarwal. K and Du. J, 2013. Hydraulic fracture geomechanics and microseismic-source mechanisms, SPE Journal, 18(04), 766-780

Yu. H, and Zhang. H, 2013. Detecting low frequency seismic signals from surface microseismic monitoring of hydraulic fracturing of a tight sand-gas reservoirs, Poster at the 2013 AGU annual meeting, San Francisco, CA, 8-13 December

Zoback. M.D, Kohli. A, Das. I and McClure. M, 2012. The importance of slow slip on faults during hydraulic fracturing stimulation of shale gas reservoirs, Paper presented at The Americas Unconventional resources conference, Pittsburgh, Pennsylvania, 5-7 June, Society of Petroleum Engineers, 155476

Zhang. H, Nadeau. R.M and Toksoz. M.N, 2010. Locating non-volcanic tremors beneath the San Andreas Fault using a station-pair double-difference location method. Geophys. Res. Lett. 37, L13304, doi:10.1029/2010GL043577